Co-Ni-arsenide mineralisation in the Bou Azzer district (Anti-Atlas, Morocco): genetic model and tectonic implications

Tourneur Enora, Alain Chauvet, Kouzmanov Kalin, Johann Tuduri, Paquez Camille, Sizaret Stanislas, Karfal Abdelhak, Moundi Younes, El Hassani Abdelfattah

HAL Id: insu-03183857
https://insu.hal.science/insu-03183857

Submitted on 29 Mar 2021

Journal Pre-proofs

Co-Ni-arsenide mineralisation in the Bou Azzer district (Anti-Atlas, Morocco): genetic model and tectonic implications

Tourneur Enora, Chauvet Alain, Kouzmanov Kalin, Tuduri Johann, Paquez Camille, Sizaret Stanislas, Karfal Abdelhak, Moundi Younes, El Hassani Abdelfattah
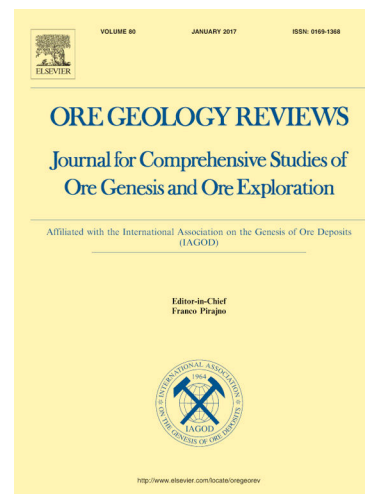
1   **Co-Ni-arsenide mineralisation in the Bou Azzer district (Anti-Atlas, Morocco): genetic**

2   **model and tectonic implications**

3

4   Tourneur Enora[1]; Chauvet Alain[1]; Kouzmanov Kalin[2]; Tuduri Johann[3,4]; Paquez Camille[5,6],

5   Sizaret Stanislas[4]; Karfal Abdelhak[7]; Moundi Younes[7]; El Hassani Abdelfattah[7]

6

7   [1]: UMR 5243, Géosciences Montpellier, University of Montpellier, University of Antilles,

8   CNRS, Montpellier, France

9   [2]: Department of Earth sciences, University of Geneva, 1205 Geneva, Switzerland

10   [3]: BRGM, F-45060 Orléans, France

11   [4]: ISTO, UMR7327, University of Orléans, CNRS, BRGM, F-45071 Orléans, France

12   [5]: Géosciences Réunion (LSTUR), University of La Réunion, 15, Avenue René Cassin, CS

13   92003, 97744 Saint Denis Cedex 9

14   [6]: Institut de physique du globe de Paris, University of Paris, CNRS, F-75005 Paris, France

15   [7]: Managem Group and CTT, Twin Centre-Tour A, BP16016, Casablanca, Morocco

16

17

18   **Abstract**

19

20   The two main types of mineralisation in the Co-Ni-As Bou Azzer district, i.e., "contact"

21   mineralisation" and "cross-cutting" structures have been re-defined based on new field, structural,

22   textural and mineralogical observations. The main orebodies consists of elongated lenses of massive

23   Ni-Co-Fe arsenide minerals. These lenses occur in a core of carbonate or siliceous gangue and are

24   almost exclusively located along the contact between serpentinite and a quartz diorite intrusion. Vein

25   systems, cross-cutting the different lithologies, are ore-bearing only along segments in contact with

26   the serpentinite and/or the massive mineralisation. The two orebody types share a rather similar

27   mineralisation history, starting with a Ni-rich arsenide stage (mainly expressed within the massive

28   mineralisation), followed by a massive Co-arsenide stage recognised in both mineralisation styles, and

29   ending with Fe-rich arsenide and base metal sulphide stage.

30   Detailed field observations, microstructural, tectonic, textural and mineralogical analyses led

31   us to propose a genetic model for the Bou Azzer ore district in which massive mineralisation was

32   formed by alteration and transformation of previously formed breccia levels composed of serpentinite

33   (transformed to gangue) and magnetite/spinel (transformed to Co-Ni arsenide minerals) fragments.

34   Inversely, a tectono-hydrothermal event controlled by a NE oriented transtension generated the vein

35   system, associated certainly with partial leaching and reconcentration of metals from the massive

36   mineralisation because veins are principally mineralised when crossing massive orebodies. We

37   discuss a possible temporal continuum between the two mineralisation styles: massive mineralisation,

38 coeval with serpentinisation (serpentine neoformation), is related to the transformation of brecciated
39 lenses and vein mineralisation is formed as an infill of large fractures during transtensive tectonics.
40 This model has significant tectonic implications, because serpentinite breccia lenses, favourable high-
41 permeability environment for the massive mineralisation formation, can be compared to ophicalcic
42 rocks developed in a context of mantle exhumation by detachment. Two types of textures can be
43 differentiated within the massive mineralisation: i) Brecciated Massive Mineralisation, developed in
44 the core of ophicalcic levels, and ii) Laminated Massive Mineralisation, supposed to form within
45 ancient mylonitic serpentinite levels corresponding to intensive deformation zones. Although the
46 geodynamic significance will not be addressed in this article, we propose and discuss an alternative
47 model in which the presence of exhumed mantle rocks allows the formation of specific massive
48 arsenide deposits.

49

50 **Keywords:** Co-Ni-As (-Au-Ag) Bou Azzer district; Hydrothermalism; Serpentinite; Vein;
51 Massive arsenide ores; Tectonic implications

52

53 **1. Introduction**

54 Economic concentrations of Co are almost always considered as by- or co-product of mining
55 where Co is associated with Cu and/or Ni. The only exception is the Bou Azzer Co-Ni-As (-Au-Ag)
56 district in Morocco that hosts the only mine in the world where Co is produced as a primary product.
57 No satisfying genetic model has been proposed so far in the abundant literature regarding the Bou
58 Azzer district. Five main Co deposit types are presently identified worldwide and associated to
59 different geological settings: 1) sediment-hosted stratiform Cu-Co deposits such as the Central
60 African Copper Belt in DRC and Zambia in which Cu and Co are mostly concentrated by diagenetic
61 processes (Cailteux et al., 2005; Hitzman et al., 2012); 2) magmatic sulphide deposits such as the
62 giant Noril'sk-Talnakh, Sudbury and Kambalda Ni-Cu (-PGE-Co) deposits in Russia, Canada and
63 Australia, respectively (Arndt et al., 2005; Naldrett, 2005); 3) secondary concentrations within
64 lateritic profiles, such as the Koniambo Ni (-Co) deposit, in New Caledonia (Freyssinet et al., 2005;
65 Butt and Cluzel, 2013); 4) Mn-nodules and Co-rich crusts on the oceanic seafloor (Manheim and
66 Lane-Bostwick, 1988; Hein and Koschinsky, 2014); and 5) the five-element hydrothermal vein type
67 (Bi-Co-Ni-Ag-As$\pm$U), whose formation is related to the involvement of methane as reducing agent
68 with the circulation of connate brines, in crustal thinning environments in continental rifting and
69 crustal thinning environments (Bastin, 1939; Kissin, 1992; Markl et al., 2016; Burisch et al., 2017).
70 Recent works also tentatively suggest (Dolansky, 2007; Burisch et al., 2017), mainly based on
71 similarities in the mineral assemblage and fluid signatures that the Bou Azzer district may belong to
72 the five-element veins deposit type.

73 The Bou Azzer mining district hosts an enigmatic type of Co-Ni-As (-Au-Ag) mineralisation
74 located at the vicinity of hydrated ultramafic rock complex (serpentinite) (Leblanc, 1975; Saquaque et

75   al., 1989; Ennaciri, 1995; Hefferan et al., 2000, Kreissl et al., 2018; Ikenne et al., 2020). Although the

76   paragenesis is rather well-known (Leblanc and Billaud, 1982; Ennaciri, 1995; Ennaciri et al., 1995;

77   Ahmed et al., 2009; Gervilla et al., 2012), the mode of formation and the structural constraints on the

78   mineralisation remain unsolved so far. Indeed, although recent models are based on hot brines

79   circulation within the basement rocks during a major extensional tectonic episode at the end of the

80   Variscan orogeny (e.g. Essarraj et al., 2005, Oberthür et al., 2009), some other assumptions argue for

81   a five-element veins deposit type (Burisch et al., 2017), suggest the deposits may have been initiated

82   at high-temperature (>500°C, Gervilla et al., 2012) or may be also polyphase during the

83   Neoproterozoic orogeny (Leblanc, 1975; Ennaciri et al., 1997; Tourneur et al., 2019).

84   Most of the authors agree that serpentinite rocks are the source for Co and Ni, leached and

85   concentrated by hydrothermal fluid circulation, because the main ore bodies are hosted at the vicinity

86   of a serpentinite complex (e.g. Leblanc, 1975; Ennaciri, 1995). However, the significance of the

87   geodynamic context in terms of prerequisite for ore formation in this particular environment has never

88   been addressed so far and structural constraints remain strongly lacking in all studies devoted to the

89   Bou Azzer district. Recently, serpentinite occurrences worldwide have been described in tectonic

90   environments where ultramafic mantle rocks are exhumed either in intra-continental extensional

91   setting (Lagabrielle and Bodinier, 2008), or in hyper-extended rift margins at the ocean–continent

92   transition (OCT; Boillot et al., 1987; Manatschal, 2004, Manatschal et al., 2006), among others.

93   Mostly, serpentinisation occurs because of seawater circulation through the underlying mantle, and

94   this process shares some common features with the formation of seafloor and sub-seafloor massive

95   sulphide deposits (Richardson, 1987; Alt, 1995; Alt et al., 1996). In this last example, percolating

96   seawater interacts with the oceanic crust mainly composed by gabbro and basalt in order to form

97   massive sulphide mineral accumulations enriched in Cu, Zn, Pb, Au, and Ag. However, it has been

98   recently demonstrated that, in the setting of mid-ocean ridges, ultramafic rocks may also exhumed

99   along slow spreading ridges and host black smokers-like hydrothermalism yielding Cu-Fe-Ni-Co-Zn-

100   rich ore occurrences (Coltat et al., 2019). No example of a similar process involving leaching and

101   hydrothermal alteration of the mantle has been discussed and proposed so far for the Bou Azzer Co-

102   Ni-As (-Au-Ag) district.

103   This paper integrates the results of a field study and structural, textural, mineralogical, and

104   geochemical analyses of the Co-Ni-As (-Au-Ag) mineralisation at Bou Azzer. A model of formation

105   is proposed and discussed taking into account the various mineralisation types, their distribution and

106   specific geometry, as well as their mineralogical characteristics. It is also discussed if both

107   mineralisation styles (massive lenses and veins) could have formed during continuous mineralisation

108   events. The continuity is suggested by similar paragenetic sequence beginning with a Co-arsenide

109   stage in both mineralisation types. However, the structural context of formation differs from

110   emplacement in permeable and brecciated zones between serpentinite, quartz diorite and Upper

111   Neoproterozoic volcanic rocks for the massive bodies, and ore formation in large fractures for the vein

112 mineralisation. The role and the significance of several parameters such as pre-existing serpentinite
113 breccias along extensional fault/detachment, in-situ transformation processes allowing the formation
114 of Co-Ni minerals at the expense of spinel/magnetite or significance of serpentinite as a major
115 contributor to the leaching, transport and capture of the metallic phases have been highlighted.
116 Finally, a tentative of integration of the Bou Azzer district in a new model of formation of "Massive
117 Arsenides" alternative that involved hydrothermal fluid circulation in an ultramafic rock complex is
118 proposed and discussed. Such a revisited ore-forming model constitutes a key for future exploration
119 targeting for Co-Ni deposits essentially due to the new definition of orebody characteristics and
120 geometry.

121

122 ## 2. Geological setting

123 ### 2.1. The Moroccan Anti-Atlas

124 The Moroccan Anti-Atlas is located in the southern part of Morocco and belongs to the
125 northern edge of the West African Craton (WAC) and bordered to the north by the South-Atlasic
126 Fault (Fig. 1). It comprises a succession of inliers that are broadly oriented WSW/ENE and
127 characterised by Proterozoic cores overlain by Palaeozoic (mostly Cambrian) sedimentary rocks
128 (Choubert, 1963). The Major Anti-Atlas fault (MAAF) separates two domains: the eastern domain
129 including the Jbel Saghro, Siroua and Ougnat inliers, whereas the western domain includes nearly 10
130 inliers. The Bou Azzer-El Graara thus occupies a central position in the Anti-Atlas and is located
131 exactly along the MAAF (Fig. 1). Field relationships also suggest that the Eastern Anti-Atlas only
132 exposes Neoproterozoic terranes, while the Western Anti-Atlas exposes a Palaeoproterozoic basement
133 overlain or intruded by Neoproterozoic sedimentary, volcanoclastic and granitoid rocks (Hollard et
134 al., 1985). Four orogenic cycles affected the Anti-Atlas area during the Palaeoproterozoic (Eburnean:
135 Barbey et al., 2004; Thomas et al., 2004; Ennih and Liégeois, 2001), the Neoproterozoic (Panafrican:
136 Gasquet et al., 2005; Tuduri et al., 2018a), Palaeozoic (Variscan: Burkhard et al., 2006) and the
137 Caenozoic (Alpine: Missenard et al., 2006). The Proterozoic events, mostly concerned by this study,
138 are the most significant and according to Choubert (1945) and Choubert and Faure-Muret (1980), they
139 have been historically divided into three main lithostratigraphic units called Precambrian I (PI),
140 Precambrian II (PII) and Precambrian III (PIII) then grouped in Supergroups, Groups, Subgroups,
141 Formations, Members and Suites with local names and geographical justifications (Thomas et al.,
142 2004), fact that not really simplified the geological understanding in our opinion. Indeed, we have
143 chosen here to present the lithology with the ancient nomenclature followed by a recent proposition of
144 simplification by Tuduri et al. (2018a).

145 Although PI terranes were previously attributed to the Palaeoproterozoic, some have been
146 reinterpreted as Neoproterozoic in age, like PII and PIII. PI is essentially made of Palaeoproterozoic

147 crystalline rocks and is only observed in the Western Anti-Atlas (Ennih and Liegeois, 2001). The PII

148 units are composed of grauwackes, quartzites and metasediments in which PII-related granitoids

149 emplaced. The ophiolitic complexes of Bou Azzer and Siroua are also attributed to PII formations

150 (Leblanc, 1975; Choubert and Faure-Muret, 1980). PIII formations consist of late volcanic units that

151 overly PI and PII. They are represented by the Ouarzazate supergroup mainly composed of

152 ignimbrites (Thomas et al., 2004; Blein et al., 2014). A new subdivision into two complexes (lower

153 and upper) has been recently proposed by Tuduri (2005) and Tuduri et al. (2018a) and appears more

154 appropriate for linking the sedimentary, volcanic and plutonic rocks to the two tectono-magmatic

155 events that affected the Anti-Atlas. The term "complex" is herein employed because the two

156 Neoproterozoic events that affected the Anti-Atlas cannot be described as classical orogenic events

157 but more likely as an association between volcanism, magmatism and tectonics that strongly

158 influences the nature of the lithologies. The particularity of these events, with strong influence of

159 magmatism, low- to medium-grade metamorphism and deformation, justifies the distinction from

160 classic orogenic phases. Indeed, the main tectono-magmatic events that characterise the

161 Neoproterozoic deformation are: i) a first magmatic-tectonic event (in the lower complex) mainly

162 associated with massive high-K calc-alkaline magmatism taking place in the core of weakly deformed

163 meta-sedimentary complexes controlled by a transpressive tectonics (e.g., Choubert, 1963; Thomas et

164 al., 2004; Gasquet et al., 2005; Tuduri, 2005; Walsh et al., 2012; Tuduri et al., 2018a,b); ii) a

165 transtensive deformation (in the upper complex) associated with periods of intense silicic volcanism

166 (multiple ash-flow caldera-forming eruptions), magmatism and volcano-sedimentary formations

167 (Gasquet et al., 2005; Walsh et al., 2012; Tuduri et al., 2018a). Such ignimbritic sequences

168 unconformably overlay the deformed lower complex. Indeed, these complexes are separated by a

169 major unconformity that is associated with changes in the tectonic setting - between the

170 compressional character of the lower complex (transpressional tectonics) and the extensional

171 character of the upper one (transtensional tectonics)(Tuduri et al., 2018a).

172   In both the Siroua and Bou Azzer inliers, an uncertainty remains about the early occurrence of

173 obduction and oceanic basin closure (suture zone) due to the supposed existence of one or two

174 subduction zones. Several geodynamic interpretations have been proposed and discussed on this

175 crucial point of the Neoproterozoic Anti-Atlas evolution (Gasquet et al., 2005; Bousquet et al., 2008;

176 El Hadi et al., 2010; Walsh et al., 2012; Triantafyllou et al., 2018) but consensus has never been

177 reached (see below).

178

179   2.2. The Bou Azzer inlier

180   Located in the central part of the Moroccan Anti-Atlas (Fig. 1), the Bou Azzer-El Graara

181 inlier represents one the most famous inliers in Morocco, because first description of a Proterozoic

182   oceanic lithosphere was made there (Leblanc, 1975) and also because of its spectacular Co-Ni-As
183   mineralisation. The Bou Azzer inlier has been defined as an ophiolitic complex supposed to be a
184   Neoproterozoic suture zone (Leblanc, 1975, 1976, 1981; Bodinier et al., 1984; Gahlan et al., 2006).
185   The inlier is parallel to the MAAF (Fig. 1b), and some faults with similar orientation were assigned to
186   this major Anti-Atlas fault. The inlier is characterised by large amounts of serpentinised ultramafic
187   rocks, originally mantle harzburgites and dunites, associated with gabbro and basaltic pillow lavas
188   (Leblanc, 1975, 1976, 1981; Bodinier et al., 1984; Gahlan et al., 2006). The ultramafic units are
189   surrounded by: i) a Cryogenian volcanic arc complex that was emplaced at *ca.* 770-760 Ma, and ii)
190   Ediacaran volcanic and volcanoclastic rocks including the Ouarzazate supergroup and then
191   infracambrian sedimentary sequences (Thomas et al., 2004; Walsh et al., 2012 ; Blein et al., 2014).
192   There, the structural pattern is assumed to follow the closure of an ocean that may have driven to the
193   obduction of the ophiolitic unit during a period bracketed between 640 and 770 Ma (Clauer, 1976;
194   Leblanc, 1981; Thomas et al., 2004; Samson et al., 2004; Blein et al., 2014). Following the formation
195   of the ophiolitic unit, the lower complex sequences consisting of deformed metavolcanic and
196   metasedimentary rocks, that represent a late orogenic detrital sequence, were emplaced (the Bou
197   Lbarod and Tiddiline groups). The latter are intruded by high-K calc-alkaline plutons of granodiorite,
198   quartz diorite and gabbro at *ca.* 650- 630 Ma (Thomas et al., 2004; Inglis et al., 2005; El Hadi et al.,
199   2010). The upper complex is characterised by numerous volcanic sheets, mostly ignimbritic,
200   belonging to the Ouarzazate supergroup and deposited during a long-lived extensional-transtensional
201   stage that began around 585-580 Ma and built up until 550-540 Ma (Mifdal and Peucat, 1985;
202   Thomas et al., 2004; Blein et al., 2014; Tuduri et al., 2018a). Most of these rocks are composed of
203   dacitic to rhyolitic ignimbrites and andesitic tuffs and overly all the Precambrian units of the Bou
204   Azzer inlier. Calc-alkaline to high–K plutonic rocks continued to intrude these volcanoclastic units
205   (Thomas et al., 2004). Both the lower and upper complex units were affected by greenschist facies
206   metamorphism (Bodinier et al., 1984; Wafik et al., 2001). A sedimentary cover sequence composed of
207   conglomerates and carbonate rocks overlies all the units and marks the transition to the
208   Precambrian/Cambrian (Pouit, 1966; Bouchta et al., 1977; Tucker, 1986; Latham and Riding, 1990;
209   Gasquet et al., 2005). This unit has been locally named the Adoudounian formation or, more recently,
210   the Taroudant group.

211

212   **2.3. The Bou Azzer Co-Ni-As (-Au-Ag-Cu) district**

213   Three major mining districts can be defined within the Bou Azzer inlier (Fig. 1C). The Bou
214   Azzer Co-Ni-As (-Au-Ag) district occurs in the NW and central parts and includes several dispersed
215   ore deposits all related to serpentinite massifs (e.g. *Taghouni*, *Bou Azzer East*, *Aghbar*, *Tamdrost*,
216   *Ambed, Aït Ahmane* and the Ag-rich *Tizi* one, Fig. 2). The Bleida Au (-Pt-Pd) district is located in the

217 south-eastern part. The third district is defined by the appearance of several small Cu-rich occurrences
218 in the infracambrian sedimentary cover (El Ghorfi et al., 2006; Bourque et al., 2014; Maacha et al.,
219 2015). The entire Co-Ni-As (-Au-Ag) Bou Azzer district is operated by the Compagnie de Tifnout
220 Tiranimine (CTT), a subsidiary of Managem, a Moroccan industrial mining group.

221 Three main ore deposit types have been described in the Co-Ni-As (-Au-Ag) Bou Azzer
222 district (Leblanc and Lbouabi, 1988; Ennaciri, 1995; Ennaciri et al., 1995b; Maacha et al., 2012): i)
223 Co-Ni arsenide "contact" mineralisation as massive lenses located at the contact between serpentinite
224 and quartz diorite and sometimes along the contact with the Upper Neoproterozoic volcanic rocks of
225 the Ouarzazate supergroup; ii) Co-rich veins "cross-cutting" all lithologies; and iii) Ag-rich
226 "stockwork" zones emplaced along the contact aureole of the quartz diorite pluton within the
227 serpentinite. Such a contact aureole is characterised by the following mineral assemblage: prehnite-
228 calcite-epidote-garnet-clinopyroxene, that represents a Mg-Ca±Mn metasomatic rock associated with
229 rodingite formation (Leblanc and Lbouabi, 1988; Essarraj et al., 2005; Borisenko et al., 2014).

230 Five mineralisation stages have been defined at Bou Azzer (Leblanc, 1975; Ennaciri, 1995;
231 Ennaciri et al., 1996; Ahmed et al., 2009): i) Ni-arsenide stage, mainly consisting of nickeline - NiAs
232 and rammelsbergite - $NiAs_2$; ii) Co-arsenide stage marked by precipitation of safflorite -
233 $(Co,Fe,Ni)As_2$, its monoclinic dimorph (*i.e.*, clinosafflorite) and skutterudite - $(Co,Ni)As_3$, sometimes
234 associated with scarce native gold; iii) Fe-arsenide stage characterised by loellingite - $FeAs_2$; iv)
235 sulpho-arsenide stage, consisting of gersdorffite - NiAsS, cobaltite - CoAsS and arsenopyrite – FeAsS
236 assemblage, and v) sulphide-sulphosalt stage, with a chalcopyrite - $CuFeS_2$, sphalerite - ZnS,
237 tennantite-tetrahedrite - $(Cu,Fe)_{12}As_4S_{13}$ - $(Cu,Fe)_{12}Sb_4S_{13}$ and molybdenite - MoS_2 assemblage, with
238 minor brannerite - $(U,Ca,Ce)(Ti,Fe)_2O_6$ (Oberthür et al., 2009). All assemblages are associated with
239 carbonate and/or siliceous gangue sometimes containing chlorite and talc.

240 The division into early "contact" mineralisation and late "cross-cutting" veins (also called
241 "croiseurs" in French) serves as a guide for CTT's geologists and miners for both exploration and
242 operation activities. However, no satisfying petro-structural genetic model has been proposed for the
243 formation of the economic mineralisation so far. Hereafter based on textural and mineralogical
244 arguments and the recognition of massive Co-Ni arsenide bodies in the core of the "contact"
245 mineralisation, contact mineralisation is called "massive", whereas "cross-cutting" mineralisation is
246 defined as veins or vein system. Only these two types are considered in the present study. Historically,
247 carbonated complex shells, also called "carapace d'Ambed" and siliceous complex shells, called
248 "Birbirite", are respectively composed of calcite and quartz, and were used in the district as major
249 exploration guidelines on surface (Leblanc, 1975; Fanlo et al., 2015; Maacha et al., 2015).

250 The age of the Bou Azzer deposits is still debated. Leblanc (1975) estimated the age of Bou
251 Azzer mineralisation during the Neoproterozoic, based on general arguments. Concordantly,
252 Neoproterozoic to Cambrian ages were reported by Ennaciri et al. (1996; 1997) with an U/Pb age
253 around 590-550 Ma (Ediacaran) on a single brannerite grain posterior to the Ni-and Co-rich stages.

254 Levresse (2001) published an ^{40}Ar/ ^{39}Ar age of 218 ± 8 Ma (upper Trias) on adularia from *Filon 7/5*
255 linked to the silver mineralisation described by Essarraj et al. (2005). Dolansky (2007) has also
256 provided geochronological data for brannerite from *Filon 7/5* vein system having a range of ages from
257 383 ± 7 Ma to 257 ± 8 Ma, i.e. Devonian to Permian. Oberthür et al. (2009) reported a large number
258 of ages ranging from Neoproterozoic to Palaeozoic using three different dating methods: Re-Os on
259 molybdenite, Sm-Nd on carbonates and U-Pb on brannerite. Only carbonate and brannerite gave
260 consistent upper Carboniferous ages of 308 ± 31 Ma (Sm-Nd) and 310 ± 5 Ma (U-Pb), respectively.

261

262 **3. Methods**

263 The present study relies on new field and structural data collected during two field campaigns.
264 Samples for this study were selected throughout the entire Bou Azzer mining from underground
265 workings in eleven deposits, down to a depth 510 m below surface *(Taghouni, Bou Azzer Centre -*
266 *Puit 3, Bou Azzer East - Puit 3 and Puit 6, Aghbar, Oumlil, Bouismass, Tamdrost, Aït Ahmane - Filon*
267 *53 and Zone D)*, seven quarries or surface outcrops *(Bou Azzer East, Quarry 52, Filon 55 surface,*
268 *Filon 2, Filon 7, Filon 5 and Bou Azzer Centre)* and one surface trench *(Bou Azzer East)*(Figs. 1 and
269 2, Table 1, all the sites are not represented in Figure 2). The names of some of the ore bodies are in
270 French, to keep the original names of the locations. In total, 72 polished thin sections (30 μm-thick)
271 were prepared for studying the petro-structural features of the Bou Azzer ore deposits from 14
272 massive and 48 vein ore bodies. Structural data were collected from 8 massive mineralisation sites
273 (Appendix 1.1) and 39 veins (Appendix 1.2). Direction, dip angle and dip angle orientation of each
274 measure are indicated.

275 Petrography and micro-structural study were performed using optical transmitted/reflected
276 light (TL and RL) and cathodoluminescence (CL) microscopes at the Géosciences Montpellier
277 laboratory (University of Montpellier, France) and the Department of Earth Sciences (University of
278 Geneva, Switzerland) to document the relationships between mineral phases and mineralised
279 structures.

280 Microanalysis was carried out using a FEI Quanta FEG 100 Scanning electron microscope
281 (SEM) and a Cameca SX100 electron probe microanalyser (EPMA) at the Service inter-regional
282 Microsonde-Sud of Montpellier (France). Major and minor elements were measured in silicate,
283 arsenide, sulphide and calcite grains with a beam current of 10nA and accelerating voltage of 20 keV.
284 Nine major elements were analysed for arsenide and sulphide (standards, spectral lines, and
285 spectrometers were as follows): Co (Co-metal, Kα, LLIF), Ni (Ni-metal, Kα, LLIF), Fe (Fe2O3, Kα,
286 LLIF), Cu (Cu-metal, Kα, LLIF), Zn (ZnS, Kα, LLIF), Pb (PbTe, Mα, LPET), S (FeS$_2$, Kα, LPET),
287 Ag (Ag-metal, Lα, LPET), Au (Au-metal, Mα, TAP), As (GaAs, Kα, LLIF). Total counting times
288 ranged from 60 to 240 sec. The concentrations of major elements are available in Tourneur (2019).
289 Mineral compositions (in apfu) were calculated considering a total of 3.5 atoms for the stoichiometric
290 skutterudite and 3 oxygens for calcite.

291   Automated mineral analysis and textural imaging of the studied samples were performed
292 using an FEI QEMSCAN® Quanta 650F facility at the Department of Earth Sciences, University of
293 Geneva, Switzerland. The system is equipped with two 30 mm^2 Bruker QUANTAX light-element
294 energy dispersive X-ray spectrometer (EDS) detectors. Analyses were conducted at high vacuum,
295 accelerating voltage of 25 kV, and a beam current of 10 nA on carbon-coated polished thin sections.
296 Field Image operating mode (Pirrie et al., 2004) was used for analyses. In total 221 individual fields
297 were measured per sample, with 1500 μm per field, and point spacing of 5 μm. The standard 1000
298 counts per point were acquired, yielding a limit of detection of approximately 2wt% per element for
299 mineral classifications. Measurements were performed using iMeasure v5.3.2 software and data
300 processing using iDiscover® v5.3.2 software package. Final results consist of: i) high-quality spatially
301 resolved and fully quantified mineralogical maps; ii) BSE images with identical resolution as the
302 mineralogical maps; iii) X-ray element distribution maps.

303   Serpentine minerals were analysed by Raman spectroscopy using a Renishaw Invia
304 spectrometer equipped with a Peltier-cooled silicon CCD detector using a 532 nm laser excitation
305 wavelength (laserpower 30 mW, 2400 g/mm grating, spectral resolution ~ 1 cm^{-1}) at Charles
306 Coulomb Laboratory, University of Montpellier, France. The excitation beam is provided by a
307 Stabilite 2017 Ar$^+$ laser (Spectra Physics, Newport Corporation) at 514.53 nm and a power of 200
308 mW (resulting in ~20 mW at sample), focused on the sample surface using a x100 objective
309 (Olympus). Two acquisitions were accumulated to provide a high-definition spectrum. To
310 characterize the bands in the Raman spectra and identify the phases present, the online database of the
311 French Society of Mineralogy and Crystallography and the software CrystalSleuth with the RRUFF
312 Project database (Downs, 2006) were used (Appendix 2). Raw data were processed using LabSpec
313 software designed for the Jobin-Yvon Horiba LabRAM instruments.

314

315   **4. Structural and macroscopic study**

316   **4.1. General features**

317   The 3D model in Figure 2 summarizes the distribution of geological units, tectonic contacts
318 and highlights the relationships, laterally and at depth, between the two major Co-Ni-As ore body
319 types (massive ore and veins) in the deposits from the Bou Azzer district. Figure 2 was built including
320 field observations at the main mining sites and quarries studied (Table 1).

321   The ultramafic units of Bou Azzer are composed of an ancient oceanic crust (mafic dykes,
322 layered gabbro, diabase, basalt and pillow lavas), serpentinised upper mantle and granitoid plutons
323 (Leblanc, 1975). Serpentinite appears as discontinuous, up 10 km-long, lenses and occur always as
324 central dome structure with north and south contacts dipping to the north and the south, respectively
325 (Fig. 2). They are surrounded by the volcanic rocks of the upper complex in the north and by mafic

326   rocks in the south, certainly relicts of an ancient oceanic crust (Beraaouz et al., 2004). Most of the
327   exploited deposits are also located south of these domes (see above), whatever their typology is
328   (massive or veins) and along the contact between serpentinite and quartz diorite (Fig. 2).Normal fault
329   motion was observed between serpentinite and the carbonated complex shell at the *Ambed* site (Fig.
330   3A). The quartz diorite intrusion crops out always south of the serpentinite (Fig. 2). Its relationship
331   with serpentinite is not clear because the contact generally appears tectonic. However, an intrusive
332   character has also been demonstrated, at least within the mafic rocks (Fig. 3B).

333   Two main structural directions exist: the N110°E-120°E general trend of the lithological units
334   (Appendix 1.1) and the NNE crossing faults (see also Figs. 4B-D; Appendix 1.2). The massive bodies
335   occur always parallel to the N110°E contact, except at *Bou Azzer East* (*BAE*), *Bou Azzer Centre*
336   (*BAC*), *Bouismass* and *Aghbar* where massive mineralisation can occur along roughly NS trends (Fig.
337   2; Appendix 1.1). Inversely, all mineralised veins occur along the NNE faults and are high-grade only
338   along segments in contact with serpentinite. The NNE faults do not cross the entire inlier, with one
339   exception - the *Igherm* fault which is the longest structure affecting also the infracambrian and
340   Cambrian units (Figs. 1 and 2). However, this is the unique fault in the area which is not mineralised,
341   even in its part that cross-cuts the serpentinite. The vein system intersects always the massive
342   mineralisation (*Bou Azzer Centre, Bou Azzer East – Puit 3 and Puit 6, Aghbar, Bouismass, Oumlil*,
343   *Tamdrost, Filon 53* at *Aït Ahmane*). One can note that these sites only occur in the western and central
344   parts of the district, domains where the serpentinised ultramafic mantle crops out, certainly because
345   mostly exhumed (Leblanc, 1975; Ennaciri et al., 1997).

346   Near the *Taghouni* and *Bou Azzer Centre* sites, the third type of mineralisation occurs as
347   disseminated silver and associated stockwork that are developed within the intrusive quartz diorite
348   (Leblanc and Lbouabi, 1988) (see location in Fig. 2). Sampling is currently impossible in this area
349   thus explaining why this type of mineralisation has not been considered in the present study.

350

351   **4.2. Surface and underground observations**

352   At surface, *serpentinite* colour is green in zones preserved from the intense carbonation and
353   talc-alteration (Fig. 3C). Serpentinite is constantly affected by a N120°E trending foliation frequently
354   underlined by magnetite-rich layers (Fig. 3C), but the foliation age remains unknown. These linear to
355   dispersed magnetite-rich beds are observed in a few places like *Bou Azzer Centre* and *Bou Azzer East*
356   *- Puit 3*, for example. The significance of such magnetite-rich structures will be discussed further.
357   Close to the contact, the serpentinite texture is difficult to recognize but several locations show the
358   presence of breccia with serpentinite fragments (Fig. 4A).

359   The *quartz diorite* body shows a greyish to greenish colour and feldspar and quartz grains are
360   recognisable. Albitisation, chloritisation, epidote-rich and titanite/calcite mineral alterations affect this

rock. Disseminated ore minerals were observed but not determined at this scale. As already stated, field relationships between serpentinite and quartz diorite intrusion are not easy to define. However, several observations suggest that quartz diorite is an intrusive body (Fig. 3B). When not mineralised and occupied by massive lenses, the contact between serpentinite and quartz diorite can show three aspects: i) underlined by mafic units or dykes (Fig. 3B); ii) underlined by red levels with prehnite-calcite-epidote-garnet-clinopyroxene minerals that have been attributed to some rodingite levels supposed to represent a by-product of the serpentinisation process or maybe the effect of the contact metamorphism between serpentinite and magmatic rocks (Fig. 3D; Leblanc and Lbouabi, 1988); iii) linear with a white alteration halo (Fig. 3E). We assume that mafic dykes could be the protolith of the rodingite levels.

All structures belonging to the *vein system* intersect the whole geological units including the massive ore and may reach several hundred metres in length (Figs. 4B-D). They are filled mainly by quartz and/or carbonate, like in the *Aghbar* sector where one can observe a several metres-large left-lateral pull apart only filled by calcite and quartz (Fig. 4B). Quartz and calcite infill is ubiquitous within all vein systems at surface, either close to or far from the mineralised areas. Veins at surface comprise economic mineralisation only close to the serpentinite contact. As illustrated at *Bou Azzer Centre*, veins can exhibit two main orientations N60°E (i.e., *Filon* 7) and N10°E (i.e., *Filon* 5) (Fig. 4C). They meet together more to the south following the orientation of *Filon 7* (Fig. 4C). At the *Quarry 52* (see location on Fig. 2), massive mineralisation classically separates the serpentinite from the quartz diorite and is expressed by the numerous carbonate and siliceous complex shells characteristic for the studied area (Fig. 4E). Thus the chronology between the two systems is here confirmed because massive bodies are systematically cross-cut by veins (Fig. 4E). Numerous pockets filled by coarse-grained, euhedral calcite, are also systematically observed (Fig. 4A).

At depth, most of the massive mineralisation consists of elongated orebodies of Co-Ni-Fe arsenide, 2 to 20 metres-thick, 15 to 30 metres-long, systematically hosted in a complex quartz/carbonate gangue and observed mainly along the contact between serpentinite and quartz diorite (Figs. 5A-B). Because of its stratabound nature, no kinematic information was recordedabout the massive mineralisation. Euhedral nickeline, skutterudite and loellingite can be observed sometimes in galleries. At this scale, gangue texture is frequently massive and seems euhedral, no matter of its nature, i.e., carbonate or siliceous (Figs. 5A-B). Massive siliceous gangue is composed of quartz, chlorite, fragments of spinel and chalcopyrite. The carbonate gangue is the most abundant and shows three types of textures: i) laminated texture with carbonate/chlorite assemblage, ii) granular texture with blueish calcite (Fig. 5A) and iii) euhedral texture with white calcite and dolomite. No chronological relationships between the three textures have been determined. These textures arise some questions about the nature of the massive mineralisation protolith. Note that serpentinite fragments were frequently observed in the carbonated gangue.

398   The veins are exploited for Co and represent high-angle structures remarkably exposed
399   underground. The veins are 2 to 60 cm-thick, and mineralised for about 20 metres, horizontally, only
400   in the segments hosted within the quartz diorite. The vein system is difficult to follow inside the
401   serpentinite where the large vein seems replaced by numerous thinner and barren fractures (Fig. 6A).
402   In contrast with the massive mineralisation, the veins show a large variety of internal textures with
403   dominant breccia, lamination, massive or comb-type infill (Fig. 5C). Minerals involved are quartz,
404   Co-Fe minerals and late yellow euhedral calcite or dolomite that frequently surrounds fragments of
405   quartz diorite and/or fragments of mineralisation (Fig. 5C). The different textures described above are
406   equally represented in veins and their distribution results from their location: i) breccias are
407   specifically located in pull-apart structures, ii) laminated textures characterise regular segments with
408   homogeneous thickness and iii) comb-type infill is encountered in open-space structures. At depth
409   also, numerous metre-scale pockets with coarse-grained euhedral carbonate infill, similar to the one
410   observed at surface (Fig. 4A) are also frequently observed (Fig. 5D). They have the same
411   mineralogical characteristics as the vein systems and are supposed to be formed during the same
412   event. Kinematic indicators observed in the mineralised faults are summarised in the next section.

413   The different types of structures, i.e. the massive mineralisation, the vein system and
414   associated pockets, are compared between surface outcrops and underground workings at the scale of
415   the ore deposit as illustrated in Figure 6, in complement to Figure 2 that only shows their distribution
416   at surface and at depth. Their main features can be summarised as follows:

417   -   The orebody geometry is similar at surface and at depth. Both mineralisation styles show
418   similar size (Fig. 6A) and orientation (Fig. 6B).
419   -   Although massive mineralisation is clearly recognisable at depth, its characteristics at surface
420   are questionable. It appears, as represented in Figure 6A, that the carbonated complex shells
421   (carapace) or siliceous complex shells (birbirite) are the surface equivalent of the massive
422   mineralisation at depth. However, these bodies are frequently oxidised at surface, having very
423   dark colours.
424   -   Mafic dykes are systematically observed at the limit between serpentinite and quartz diorite.
425   They have the same position and orientation as the massive orebodies, but neither
426   mineralisation, nor alteration, were observed associated with them.

427

428   ### 4.3. Kinematic constraints

429   Because of the massive texture of the ore it is rather difficult to conduct kinematic
430   observations in the lenticular orebodies. These structures strike N120°E, parallel to the Major Anti-
431   Atlas Fault (MAAF) which cross-cut the Bou Azzer inlier and dip mostly to the NE or SW (Figs. 1, 2,
432   4, and 6). Inversely, the vein system exhibits abundant criteria of motion that diverge following the

433 vein orientation. Stereonet diagrams of Figure 6B demonstrate that veins mainly trend from N10° to

434 N70°E with a main dipping to W or NW, respectively and values close to 60-80°.

435   A normal vertical motion is observed resulting in pull-apart structures (Figs. 7A-B and 8).

436 Horizontally, both dextral and left-lateral motions are observed as indicated in the stereoplots of the

437 Figure 6B in which dextral planes are in red whereas left-lateral ones are in black. Indeed, the veins

438 trending close to N-S exhibit dextral sense of motion (Figs. 7C and 8) whereas the ones trending

439 N70°E are associated with left-lateral motion (Fig. 7D). The fact that numerous textures are equally

440 represented indicates that the vein structures were also active as fault zones and the distribution of the

441 different textures depends on their location with respect to the fault zone. This explains why breccias

442 are specifically located in normal motion pull-apart structures (Fig. 7D) whereas laminated textures

443 characterise regular segments with homogeneous thickness with comb-type infill (Fig. 7A).

444

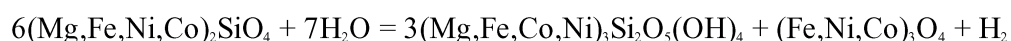## 5. Mineralogy and microscopic texture

446   Differently to the five stages of the literature, three main mineralisation stages (colours in Fig.

447 9) have been distinguished and described below. Textural features and relative major element (Co, Ni,

448 Fe, As, and S) abundances have been also added.

5.1. Host rocks mineralogy

450   The *quartz diorite* is mostly composed of albite, K-feldspar, pyroxene, apatite, quartz,

451 oriented chloritised biotite and muscovite, rare epidote and zircon (grey in Fig. 9). Because

452 plagioclase, pyroxene and biotite exhibit a rather subhedral forms, a hypidiomorphic granular texture

453 is defined (Fig. 10A). Foliation is marked by white mica and secondary chlorite. Plagioclase, which

454 has variable size, is albitic in composition (Ab# = 0.92-0.99) and occurs as euhedral to subhedral

455 grains with typical polysynthetic twins (Tourneur, 2019). Apatite, 10 - 250 μm in size, appears as

456 euhedral to rounded crystals showing zonation and altered rims in CL images. Near the veins, apatite

457 is spatially associated with chlorite and loellingite, cut by k-feldspar veinlets (Fig. 10A).

458   The *serpentine* (grey in Fig. 9) composition is intermediate between lizardite and chrysotile,

459 based on Raman micro-spectroscopy measurements (Appendix 2). However, lizardite is the major

460 mineral in serpentinite, whereas fibrous chrysotile occurs as an infill in some veins close to the

461 contact between serpentinite and massive orebodies (Fig. 10B). Serpentinite rocks are characterised

462 by the occurrence of bastite showing the shape of pyroxene grains resisting to serpentinisation and

463 associated pervasive carbonation (Leblanc and Lbouabi, 1988; Ahmed et al., 2005). Rammelsbergite

464 (Ram) and nickeline (Nk1) disseminations were found within the serpentinite, close to the massive

465 bodies (Figs. 10B-C). These minerals are the only expression of the mineralisation within the

466 serpentinite (Fig. 10B). Scarce sulphides and sulfo-arsenides (chalcopyrite, sphalerite, galena,

467 gersdorffite, bornite, chalcocite, digenite, Tnt-Ttr, arsenopyrite, cobaltite) can also be observed in the

468   serpentinite (Fig. 11A). As reported by Gahlan et al. (2006) and Fanlo et al. (2015), two types of

469   spinels/magnetite are commonly observed in the Bou Azzer serpentinite: i) disseminated Cr-rich

470   spinels (Fig. 10E) showing margins enriched in magnetite and ii) magnetite beds mostly located far

471   from the massive mineralisation (Fig. 3C). Following equation (1), iron can be released from olivine

472   during serpentinisation allowing the formation of magnetite along the border of Cr-spinel.

473   (1) Olivine + H_2O = Serpentine + Magnetite + H_2

474           $6(Mg,Fe,Ni,Co)_2SiO_4 + 7H_2O = 3(Mg,Fe,Co,Ni)_3Si_2O_5(OH)_4 + (Fe,Ni,Co)_3O_4 + H_2$

475

5.2. Mineralogy and mineral chemistry of the Ni-Co ore

477   The *massive Ni-Co orebodies* are characterised by two successive mineralisation stages:

478   -   The early stage of Ni-arsenides (purple in Fig. 9) consists of a first generation of

479   nickeline (Nk1, Fig. 10G) with rammelsbergite (Ram) (Figs. 10E-F and 11B-C). Note

480   that the monoarsenide (nickeline) crystallised first followed by the diarsenide

481   (rammelsbergite; Fig. 10G). When disseminated in serpentine, nickeline shows a

482   higher #Co (#Co = Co / (Co+Ni+Fe)) of 0.03 than grains from the massive

483   mineralisation where #Co is 0.005 (14 analyses; Tourneur, 2019). However,

484   rammelsbergite shows similar #Co if the mineral is disseminated in the serpentine or

485   occurs in the massive mineralisation (#Co=0.27 and 0.24, respectively; Tourneur,

486   2019).

487   -   The second stage consists of a massive Co mineralisation (green in Fig. 9). Following

488   the rammelsbergite deposition, the cobalt arsenide stage is characterised by the

489   association of a first generation of cobaltite (Cob1) with small and equidimensional

490   skutterudite (Sku1), followed by the first generation of calcite (Cal1) (Figs. 10F-G

491   and 11B-C). Then, it is characterised by the formation of a large amount of

492   skutterudite (Sku2) and final safflorite (Saf1; Figs. 10F-G-H). Using QEMSCAN

493   analysis and X-ray elemental mapping, skutterudite grains show important

494   compositional variations between Ni-rich bands and Co-rich bands, becoming

495   progressively enriched in Co, as also observed by Gervilla et al. (2012) and Ahmed et

496   al. (2009). The core of the grains has a Ni-skutterudite composition ($Ni_{0.75}Co_{0.25}As_{2.5}$)

497   whereas the rims progressively acquire a more typical skutterudite composition

498   ($Co_{0.75}Ni_{0.25}As_{2.5}$; Figs. 11B-C). ($Fe^{2+} + Ni^{2+}$) versus Co^{2+} and As^+ versus S^+ show a

499   negative correlation (Figs. 12A-B), as also noted by Dolansky (2007), Ahmed et al.

500   (2009), Gervilla et al. (2012) and Maacha et al. (2015). Figure 12 reveals variable

501   composition of cobalt and iron-nickel between skutterudite 1 formed in the

502   serpentinite and skutterudite 2 of the massive mineralisation. Sku1 has high Co values

503   (15.4-19.5 wt% Co) while Sku2 shows lower Co content (12.1-18.0 wt% Co;

504   Tourneur, 2019). Sku2 may therefore reflect a progressive evolution of the

505   mineralising system as continuum process from high Co content to Ni-Fe

506   compositions (Fig. 12B). Cob2 and Nk2 are considered as alteration minerals on Ram

507   and Sku2 because occurring as rims around the primary rammelbersgite grains and

508   along fractures (Figs. 9 and 13A).

509

510   Two different gangue associations (siliceous and carbonated) host the massive mineralisation

511   (black in Fig. 9). Note that relationship between both the siliceous and carbonated gangue was not

512   observed. The siliceous gangue is composed by a first generation of quartz (Qz1) and chlorite. It hosts

513   Co-rich arsenides, chalcopyrite and is mostly observed in surface outcrops. The carbonated gangue is

514   the most abundant and composed of calcite, dolomite, disseminated Cr-rich spinel and laminated

515   chlorite associated with Co- and Fe-arsenides. The Mg-Fe-Mn diagram of carbonate which is mostly

516   calcite in composition, integrates analyses from each structure (Fig. 12C). Calcite in the carbonated

517   gangue shows an average of #Mn = 0.46, with a homogeneous composition with Mg and Fe (see

518   Tourneur, 2019 for data). Carbonate composition from the surface "carapace" shows trend from Mg-

519   rich to Mn-rich compositions (Fig. 12C; see location of the main "carapace" in Figs. 1 and 2). In the

520   paragenetic evolution, the Ni-arsenide stage of the massive mineralisation is followed by the Co-

521   arsenide one observed in serpentinite and in the gangue. Cal2 shows a close link with Sku2 as

522   suggested by the crystallisation of Cal2 in the core of the growth bands of Sku2 (Fig. 13C).

523   Disseminated Cr-rich spinel crystals with alteration halo of magnetite (Fig. 13B), are not only hosted

524   in the serpentinite, but are also found around rammelsbergite and skutterudite 2 in the carbonated

525   gangue (Fig. 10E). Then, Lo2 formed at the edge of safflorite (Saf2), representing what we consider

526   as the Fe stage and also coeval with Cal2 (blue in Fig. 9, Fig. 10H). The base metal assemblage

527   consists of sphalerite (Sp), chalcopyrite (Ccp1), arsenopyrite (Apy1), galena (Gn) and gersdorffite

528   (Gd) in the carbonated gangue and represent the sulphide stage formed at the end of the massive

529   mineralisation paragenesis (Fig. 9).

530

531   *Veins* which are intersecting massive mineralisation and quartz diorite (Fig. 6A) exhibit a

532   complex infill with several successive stages. Infill is composed, first, of tiny to large euhedral

533   skutterudite (Sku3) associated with an early dolomite generation (Dol1), two calcite generations (Cal3

534   and Cal4), comb quartz (Qz2), cobaltite (Cob2) and late calcite (Cal5) (green in Fig. 9, Figs. 11D-E

535   and 13D). Sku3 has variable composition compared to Sku1 and Sku2 that can be easily discriminated

536   (Fig. 12B). Figure 11F shows growth banding in skutterudite 3 with Co-, Ni- and Fe-rich zones. It is

537   noteworthy that skutterudite of the veins contains non-negligible amount of Ni (Fig. 12B).

538   Disseminated and oriented cobaltite (Cob3) grains with a N160°E trend were seen between comb

539   quartz (Qz2) (Fig. 13D). Cob3 also formed along the rim of Sku3 and shows high Ni content (around

540 5 wt%; Fig. 11D) even though Ni-rich arsenide has never been reported in the vein system of Bou

541 Azzer. Star-shaped safflorite (Saf2) followed by elongated crystals or also star-shaped loellingite

542 (Lo2) are then formed as a replacement of skutterudite (Sku3), also showing variable Co and Fe

543 content (Fig. 11F). A second generation of veinlets with euhedral adularia (Adu) crystals forms

544 parallel to the earlier albite/quartz veins (Fig. 13E). Cal5 is enriched in Mg and Mn (Fig. 12C), with

545 #Mn of ~ 0.66, significantly higher than those of the massive mineralisation.

546

547 The *metric-scale pockets* (Figs. 4A) exhibit open-space fillings consisting, chronologically, of

548 quartz, carbonate and Co-Fe arsenide (Fig. 5D). They are filled by similar arsenide and sulphide

549 mineral phases to those observed in the veins: e.g. sub-euhedral Sku3 followed by aggregates of Saf2

550 and Lo2 in a quartz/chlorite gangue. A comparison between loellingite in the quartz diorite, the

551 massive mineralisation, the pockets and the veins shows that loellingite from the quartz diorite has the

552 higher Fe content (average at 26.4 %wt. of Fe) whereas loellingite from the massive mineralisation

553 and those from veins and pockets show lower values (respectively, average Fe contents of 17.5, 22

554 and 25 % wt.; see loellingite data available in Tourneur, 2019). Quartz 2 is followed by rhombohedral

555 Cal4 associated with Cob2 and sulphides (Fig. 13F). Fragments of Lo2 are observed in the gangue of

556 carbonate (Cal4), frequently in the middle of these structures (Fig. 11F). This calcite (here named

557 Cal4) has a composition similar to calcite from the veins with typical high Mn content (average #Mn=

558 0.9; Fig. 12C). Both structures, veins and pockets, contain a late sulphide stage characterised by the

559 formation of sphalerite, arsenopyrite, chalcopyrite and other accessory minerals (blue in Fig. 9).

560

561 **5.3. Texture**

562 Textural characteristics of the massive mineralisation, veins and pockets are indicated in the

563 lower part of the Figure 9. The main characteristics are the following:

564 - Massive mineralisation exhibits complex internal texture with various aspects of the

565 Ni-Co arsenides (Ram, Nk1, Sku1, Sku2). Rammelsbergite occurs as isolated grains

566 in the serpentinite (Figs. 10B and 10D) and in the carbonated/siliceous gangue (Figs.

567 10F-G). In fact, rammelsbergite occurs as massive, isolated (Figs. 10G and 11B) and

568 as euhedral feathery, sometimes dendritic and/or brecciated grains (Figs. 10F and

569 11B). Commonly, isolated rammelsbergite grains are included within massive Co-

570 arsenide (Sku2; Figs. 10F-G and 11B). High magnification imaging and elemental

571 mapping illustrates that euhedral feathery or dendritic rammelbersgite overgrows

572 earlier crystals, certainly formed on previous spinel sites (Fig. 14A). In addition,

573 Sku2, Saf2, Lo1 and Cal2 that crystallised after the first rammelsbergite generation

574 exhibit typical euhedral shapes certainly due to an open space growth or to

replacement as discussed below (Figs. 10E-G and 13C). Optical transmitted light and cathodoluminescence microscopy revealed that the carbonated gangue hosting the arsenide shows two alternating textures: i) coarse-grained rhombohedral Cal2 with clear cleavage and twinning without visible deformation (Figs. 13C and 13G), and ii) smaller-grained with a jigsaw-like geometry, typical of brecciated domains (Fig. 13G). The occurrence of large brecciated domains of arsenide (Fig. 13G) is confirmed by the serpentinite fragments (Fig. 4A) and will be discussed below (Brecciated Massive Mineralisation, BMM).

- Rarely, massive lenses exhibit a laminated texture with alternating calcite-rich layers (Cal2) and arsenide-rich ones (Fig. 10C). These textures have been called here Laminated Massive Mineralisation (LMM) to differentiate them from the BMM (see above).

- In the core of the serpentinite, three specific features occur: i) rammelsbergite and Sku2 are commonly fractured, with a serpentine infill (Figs. 10B-C); ii) inherited fragments of serpentinite can be observed (Fig. 13H), and iii) ghosts of mesh texture of calcite are observed in the carbonated gangue (Fig. 14B).

- Open-space infill textures are characteristic for the veins. Qz3 shows comb texture formed during the opening of the veins (Figs. 13D-E). Associated to comb-quartz 3, Cob2 shows a compatible texture with a potential growth toward the vein centre (Fig. 13D). Calcite from the veins occurs also as massive rhombohedral large grains (Cal4) (Fig. 13F). Inside the veins, skutterudite exhibits fractures filled by carbonates thus illustrating syntectonic infill (Fig. 11F). Fractured apatite, chlorite and loellingite have been observed also in the quartz diorite along the vein contacts.

- Mineralised pockets are observed only inside the massive mineralisation. They show also open-space filling textures with large centimetre-scale comb-quartz (Qz3), associated with Co-Fe arsenide formed along the quartz (Fig. 13F). Cal3 of the pockets shows two types of textures: large rhombohedral texture and smaller fragmented calcite. Some fragments of Lo2 are also fractured by Cal3 and then, associated with Qz3 formation.

5.4. Alteration

Alteration of the quartz diorite is common and consists in an intense chloritisation, a complete albitisation of all feldspars, an epidote-rich alteration forming green fractures spatially associated with the massive mineralised structures and a titanite/calcite (Calc6) alteration. These features are typical of sodic-calcic alteration (Fig. 9). At the contact between the serpentinite and the quartz diorite where

610   no massive mineralisation is formed, a red and compact rodingite reaction was observed (see above

611   and Fig. 3D). Serpentinite shows some talc- and carbonate- related alteration. In the massive

612   mineralisation, Ni and Co-arsenides (Cob2, Nk2 and Gd) have been observed as secondary minerals

613   around fractured rammelsbergite and Sku2 (Fig. 13A). Erythrine has been described by Leblanc

614   (1975) as a supergene alteration of Co arsenide.

615

616   **6. Discussion**

617   **6.1. Main results**

618   The new contributions of our structural, textural and mineralogical study of the Bou Azzer ore

619   system are summarized as follows:

620   1. The massive bodies, metre-scale in size and trending N120°E, are distributed along the

621   contact between serpentinite and quartz diorite (Fig. 2). The vein type mineralisation is NS to

622   N070°E trending and cross-cuts the various lithological contacts in the Bou Azzer area. The

623   system evolves from Ni-rich-(Co-Fe) in the massive bodies to Co-rich-(Ni-Fe) mineralisation

624   in the cross-cutting veins. In both systems, the mineralogical succession is the one established

625   in Figure 9 and can be summarised by three mineralogical stages: i) an arsenide Ni-rich stage

626   with rammelsbergite/nickeline developed specifically within the massive bodies, ii) an

627   arsenide Co-rich stage forming late in the massive bodies evolution and at the beginning or as

628   the main stage of the vein system, and iii) a final stage with Cu-Fe sulphides observed in both

629   systems.

630   2. Massive mineralisation is composed by a carbonated gangue, a siliceous gangue and arsenide-

631   rich bodies. The ore consists of decimetre-scale elongated bodies parallel to the

632   lithological/tectonic contact between serpentine and the hanging wall lithology (quartz diorite

633   or Precambrian volcanic rocks), whereas gangue forms lenses with complex morphology

634   surrounding the massive bodies. The gangue texture reflects the fact that these lenses are

635   certainly former breccia bodies with numerous residual fragments of serpentinite that have

636   been observed at surface, underground and also at microscopic scale. Serpentinite does not

637   occur only as fragments but also as veins and fractures (Fig. 10B) or fibrous crystals between

638   fragmented rammelsbergite (Fig. 10C). Such textures testify of serpentinisation synchronous

639   to the Co-rich mineralisation or corresponding to a late alteration and fracturing of the Co-rich

640   mineralisation.

641   3. Textures of the massive bodies can be separated in two types:

642   a. The most common texture consists of isolated lamellar rammelsbergite grains

643   encapsulated within the paragenetic succession with, successively, Cal1, Sku1, Cob1,

644   Ccp1 (Figs. 10F-G, 11B and 14);

645   b. Rarely, laminated textures are observed with alternating layers of lamellar nickeline

646   and automorphic Cal2 (Fig. 10D). Ni-rich minerals are overgrown by calcite,

647   cobaltite and skutterudite prior to the Fe-sulphide stage, when loellingite and

648   chalcopyrite precipitate. The coexistence of these two textures is further used as a

649   major criteria for constraining the formation model of the Bou Azzer mineralisation

650   (see below).

651   4. The vein system exhibits internal textures resulting from a tectonically controlled mode of

652   formation. Veins are associated with sinistral or dextral motions according to their orientation

653   (Fig. 8) and a normal motion is systematically deduced from vertical planes of observation.

654   5. Formation of metre-scale pockets in the core of the massive mineralisation is attributed to the

655   vein formation stage. These pockets are mainly characterised by large euhedral calcite that

656   form 90% of the structures but mineralisation (quartz, skutterudite, safflorite, loellingite and

657   cobaltite) is only found along the contacts or in central position of the pockets (Figs. 4A and

658   5D).

659   6. Within the quartz diorite, dissemination of arsenide minerals, and specifically loellingite,

660   developed close to the vein type mineralisation. Because these minerals are fractured by K-

661   feldspar veinlets (Fig. 10A), their formation is supposed to be earlier than the vein formation

662   event.

663   7. Within the serpentinite, close or far from to the massive bodies, Cr-spinel is replaced by or

664   transformed to magnetite (Figs. 10E and 13B; Ikenne et al., 2005; Gervilla et al., 2012; Fanlo

665   et al., 2015). It was interpreted that in the massive parts of the orebodies, Cr-spinel is totally

666   replaced by rammelsbergite or skutterudite.

667

6.2. Formation of the Bou Azzer Co-Ni-As ore mineralisation

669   We propose an integrated genetic model for the Co-Ni-As mineralisation at the Bou Azzer

670 district explaining the formation of both mineralisation types (Fig. 15).

671   1. The geological and tectonic setting that prevails during mineralisation processes is herein

672 constructed. We will demonstrate in the following model that this setting plays a significant role for

673 the mode of formation and for the geometrical/morphological constraints of the various mineralisation

674 styles in the district. Only the case of massive mineralisation developed at the contact between

675 serpentinite and quartz diorite is presented here. It has been demonstrated that massive mineralisation

676 occurs in the core of a gangue in which serpentinite fragments subsist. It is then concluded that a pre-

677 existing fault zone and its associated breccia (Tourneur et al., 2019) can represent the initial stage as

678 illustrated in Figures 15A and 15A1. Indeed, we therefore suppose an initial coexistence of laminated

679 (mylonitic zone of the fault) and brecciated parts of the pre-existing fault. We also suppose that some

680   parts of the brecciated level can contain fragments of the quartz diorite and that spinel and magnetite

681   are also present. Some domains with open space between fragments are also supposed to exist and

682   represented in white in Figure 15A.

683   2. The first stage consists of hydrothermal fluid incursion which preferentially percolated

684   along the lithological/tectonic contacts and within the highly porous brecciated area (Fig. 15B). It is

685   unknown if the fluid arrived from the upper, lateral or lower part of the system. All possibilities are

686   presented in Figure 15B (white arrows). During this stage, the two types of massive mineralisation

687   were formed, i.e., the Laminated Massive Mineralisation (LMM) within mylonitic parts of the

688   serpentinite and the Brecciated Massive Mineralisation (BMM) within the other parts. Figure 15B1

689   gives the microscopic details revealing that first rammelsbergite and nickeline form by

690   replacement/transformation of the spinel fragments and magnetite concentrations. The position of Ni-

691   minerals within the serpentinite strongly suggests that the Ni-bearing minerals replace some former

692   Cr-spinel grains or fragments (Figs. 3C and 10E). Serpentinisation was still on-going at least during

693   the earlier stages of this event as evidenced by the observation of serpentine veinlets and fibres that

694   cross-cut earlier Ni-minerals such as rammelsbergite (Figs. 10B-C). Chrysotile veins also form all

695   along the contact between serpentinite and mineralisation although this could be a later event. During

696   the following stage (Fig. 15B2), massive mineralisation precipitates around the earlier rammelsbergite

697   and nickeline and forms the massive bodies. Successive crystallisation of calcite, cobaltite and

698   skutterudite surrounds the rammelsbergite lamellar crystals (Fig. 10F). It ends with the precipitation

699   of large euhedral calcite that forms the principal carbonate gangue (Fig. 15B2). Final crystallisation of

700   sulphides and Fe-As-rich minerals is also observed, developed within both the massive bodies and

701   associated gangue, but also in the quartz diorite (Fig. 15B).

702   3. The late mineralisation stage corresponds to the emplacement of the NS to NE-SW veins

703   (Fig. 15C). A complex infill is observed and the main mineralisation is represented by skutterudite

704   fragments (Fig. 15C) and/or small cobaltite crystals formed in the core of vein-related comb quartz

705   grains (Fig. 13D). Veins are structurally controlled as illustrated by their sigmoidal shape and the

706   texture of the infill (comb quartz grains, breccia with fragments). As for the massive mineralisation,

707   this event ended by the crystallisation of sulphides and Fe-As rich minerals both within the veins but

708   also in the host quartz diorite. In parallel with vein formation, the development of metre-scale pockets

709   is observed (Fig. 15C1). These pockets formed in the core of the carbonated gangue of the massive

710   mineralisation (Fig. 5D). The pockets infill is comparable to that of the veins and exhibits, from rim to

711   core, skutterudite 2, large euhedral quartz and carbonate (that composed 90% of the structure) and

712   finally, safflorite, loellingite and the late Fe-rich sulphides. In our model, the pockets are developed in

713   favour of pre-existing zones of void left between fragments of the initial breccia (see Figs. 15A and

714   A1). The formation of these pockets, coeval to the vein system, is associated to open-space textures

715   such as euhedral quartz and carbonate crystallisation, consistent with an on-going extensional (or

716   transtensional) context.

Consequences of this integrated model are multiple. Two possibilities exist in order to explain the similar paragenesis: i) veins formed by remobilisation of the massive mineralisation during a late event; ii) vein and massive mineralisation are coeval and the difference is explained by a contrasting mode of formation (replacement/percolation/transformation for massive mineralisation and filling of fractures for veins). We will see in the next sections that the second hypothesis is here preferred even if uncertain. Effectively, except the Ni-rich stage that is characteristic of the early massive mineralisation, the paragenetic evolution of both structures (massive and vein mineralisation) is quite similar with successive Ni-Co-Fe arsenide, Co-Fe sulfo-arsenide and final Fe-rich sulphide stages (Fig. 9). The only divergence is textural thus indicating a different tectonic context for their formation as suggested in Figure 15. Massive orebodies were formed in situ, replacing pre-existing breccia bodies whereas vein systems result from aperture and formation of traps due to tectonics. Veins, which are only mineralised in the vicinity of the massive bodies, provide an evidence that their enrichment can result from the persistence of fluid-rock interaction. This observation demonstrates that veins can form during or immediately after the massive bodies (see below).

The hypothesis that massive mineralisation is developed as a replacement of pre-existing breccia zones explains the presently observed geometry and distribution of the different massive orebodies with a lot of small scale discontinuous deposits (Fig. 15). The consequences for exploration and exploitation strategy of the CTT mining company are significant and the necessity to account for some discontinuous and dispersed deposits is confirmed.

6.3. Mineralogical evolution

Because the mineralogical evolution found within both systems is similar except the presence of Ni-minerals only within the massive orebodies, we propose that, even if massive bodies are formed first, continuity may exist between the processes responsible for the formation of massive and vein mineralisation in different tectonic context. The massive mineralisation could be formed by a replacement of the brecciated contact zones between serpentinite, quartz diorite and Precambrian volcanic rocks due to hydrothermal fluids circulation. Vein system is coeval and formed by remobilisation of the massive mineralisation specifically because they are mineralised only at their contact and certainly because necessary conditions prevailed to allow the precipitation of metal-bearing fluid. The fact that late large-scale fault (the Igherm Fault, Fig.1C) cross-cutting the entire Bou Azzer domain is not mineralised confirms the close relationships, at least in time between the two systems (see above). This may confirm that P-T conditions necessary for fluid-rock interactions were still preserved during the formation of the vein system, so certainly during or later to the massive ore formation. Indeed, if later, veins would have cross-cut the Cambrian units.

751   Each structure shows similar features that explain the hydrothermal control of mineralisation
752 by the circulation of hot brines along lithological contacts (massive bodies) or faults (veins
753 system)(e.g. Enneciri et al., 1995; Essarraj et al., 2005; Ahmed et al., 2009; Burisch et al., 2017;
754 Ikenne et al., 2020; Hajar et al., 2020):

i)   Ni-Co massive mineralisation is supposed to develop by
replacement/transformation of spinel/magnetite grains of the serpentinite host rock
as illustrated in Figures 10E and 13B and already suggested in the literature
(Gervilla et al., 2012; Fanlo et al., 2015);

ii)   the carbonated gangue close to the massive mineralisation is interpreted as a
serpentinite breccia transformed by a hydrothermal fluid along the contact between
the quartz diorite, Precambrian volcanic rocks and serpentinite. The occurrence of
preserved serpentinite fragments (Fig. 13G), spinel fragments (Fig. 13B) and
maybe ghost mesh texture entirely overprinted by calcite (Figs. 14B-C) provide the
basis of this interpretation;

iii) an extensional context with low-angle detachment can lead to the formation of
open-space between fragments of the brecciated zones. Large scale pockets filled
by euhedral minerals indicate open space crystallisation, consistent with that
expected within a brecciated extensional environment;

770   Hydrothermal leaching of the host rocks seems at the origin of the remobilisation of the
771 economic elements. This has been texturally demonstrated here but would need a confirmation by
772 mass balance calculations. However, we can suppose that Ni and Co have their origin mainly from the
773 ultramafic rocks (Laubier et al., 2014), Fe from the quartz diorite or oxides and base metal elements
774 from meta-oceanic rocks or serpentinite (Leblanc and Fischer, 1990; Alt and Shanks, 1998). Also, the
775 source of such a large amount of arsenic necessary to form the Bou Azzer Co-Ni-As mineralisation
776 remains questionable. Smedley and Kinniburgh (2002) and Burisch et al. (2017) made a compilation
777 about the source of arsenic in minerals and rocks (Appendix 3). Arsenic can be concentrated within
778 various types of rocks and minerals such as Fe-oxide, apatite and magnetite but also in ultramafic,
779 sedimentary or intermediate igneous rocks (diorite, granodiorite). Following the authors, fibrous
780 magnetite (concentration up to 400 ppm), magnetite disseminated grains or veins (< 20 ppm),
781 sulphide in serpentinite (50 to 1000 ppm), Neoproterozoic granitoid intrusions (< 10 to ~ 25 ppm),
782 serpentinite (200 ppm), and volcanic rocks of the Ouarzazate supergroup (100 to 300 ppm) (Leblanc,
783 1975; Gahlan et al., 2006; Leblanc and Fischer, 1990; Beraaouz et al., 2004; Hattori et al., 2005;
784 Leblanc and Billaud, 1982, respectively) are good candidates as source rocks. However, principally
785 because the excess of As is expressed within mineralisation that occurs as a
786 replacement/transformation of relictic Cr-spinel hosted in serpentinite fragments (this study) and
787 because it has been also demonstrated that Ni and Co-rich arsenide minerals developed as a

788 replacement of relictic Cr-spinel partially bordered by magnetite (Fig. 13b; Gervilla et al., 2012; Fanlo

789 et al., 2015), the serpentinite and all accessory minerals inside are the best candidates as source for As

790 at Bou Azzer, even if the apatite of the quartz diorite cannot be excluded.

791

792 ### 6.4. Tectonic and geodynamic setting

793 One of the main results of our study is the establishment of an initial context that can explain

794 the specificity of the Bou Azzer mineralisation. Because of the preservation of numerous serpentinite

795 fragments, the initial breccia certainly formed along detachment fault contact between serpentinite

796 and quartz diorite or Precambrian volcanic rocks (i.e., Fig. 3A). Indeed, we assume that previously to

797 the mineralisation, brecciated zones with subsequent permeability may form in domains that were

798 later transformed into massive orebodies and associated gangue mineralisation. Because these

799 breccias occur as elongated pluri-metric-scale lenses systematically developed at the contact between

800 the serpentinite and other units (mainly quartz diorite), we suggest they can correspond to some pre-

801 existing fault-related polymictic sedimentary breccias developed along fault slope as already

802 suggested in the case of the French Pyrenees (Clerc et al., 2012). Indeed, these breccia outcrops can

803 be compared to the famous ophicalcite lithologies defined as brecciated and fractured peridotites with

804 a carbonate matrix (Clerc et al., 2012), as illustrated in Figure 16. We also propose that the siliceous

805 gangue was formed following similar processes but within parts dominated by quartz diorite

806 fragments. But this hypothesis has not been followed by thorough analysis. In the case of Bou Azzer,

807 it is then proposed that the location in which massive mineralisation was developed can be defined as

808 tectonic contacts. LMM and BMM types of mineralisation are then formed during the same event, but

809 depending on the position within the fault context and on the initial texture, as illustrated in Figures

810 15 and 16.

811 The nature of the fault and consequently the type of context remains questionable. It is

812 noteworthy that ophicalcite has been described mainly within extensional domains and specifically

813 within area where mantle exhumation took place (Hölker et al., 2003, Lagabrielle and Bodinier, 2008;

814 Caby, 2014). These rocks are finally intimately associated with the recent concept of a mantle

815 exhumation within extremely thinned continental margin and/or Oceanic Continent Transition (OCT).

816 The nature of the tectonic contacts and the geodynamic setting of the Bou Azzer serpentinite

817 exhumation are not subject of this study and will be re-addressed in a paper in preparation (Chauvet et

818 al., in prep.). However, it can be suggested, as a preliminary idea, that such hyper extension can be

819 developed in a back-arc position with respect to the geodynamic model proposed by Triantafyllou et

820 al. (2018). This model suggested that a north-dipping subduction may form the Tichibanine,

821 Tazigzaout and Bougmane arcs (see location in Fig. 1c), intensively affected by subsequent

822 deformation in response to the N-S trending compression. However, the lack of intensive deformation

823 in the Bou Azzer parts where serpentinite crops out may suggest that such areas can be rather affected
824 by hyper-extension that can explain the mantle exhumation helped by normal faulting with a
825 deformation extremely located close to the contact (Fig. 16) (Ishii et al., 1992; Jolivet et al., 2018).

826 The quartz-diorite body formation remains a riddle. In this study, we argue for intrusive
827 relationships (Figs. 3B and 4A). Two alternatives can be advanced. First, the quartz diorite can be the
828 result of the north-dipping subduction proposed by Triantafyllou et al. (2018). Therefore, its location
829 in the core of a hyper-extended rift more to the north is justified. Another solution would be that the
830 quartz diorite resulted from the intrinsic exhumation process as predicted by Manatschal (2004) as a
831 character of rifted margin in which mantle exhume to the sea floor.

832 Although the formation of massive mineralisation can be considered as the result of
833 replacement/transformation processes, the vein system appears clearly dependent on the tectonics.
834 Syn-tectonic infill textures associated with transcurrent/normal faulting (Fig. 7) are the main
835 arguments. NS dextral and NE sinistral conjugated vein systems are consistent with a N030°E
836 shortening direction, certainly associated with a vertical component explaining the systematic normal
837 motion (Fig. 8). Pull-apart structures are the most abundant. These motions are the ones that are
838 coeval with vein/fault formation because controlling their infill. Transtension is suggested because of
839 the systematic association between wrench motion and normal ones. Such a NE-SW shortening
840 direction during transtensive tectonics has been already suggested by Tuduri et al. (2018a), and
841 particularly as controlling the final mineralisation stage in various deposits of the Jbel Saghro, during
842 the upper complex formation. Several Au-Ag occurrences of the central Anti-Atlas of Morocco, i.e.,
843 the *Thaghassa* intrusion-related gold deposit (Tuduri et al., 2018b), the *Qal'at Mgouna*, and *Zone des*
844 *Dykes* gold indexes and the second stage of the *Imiter* silver mine are the main examples (Tuduri et
845 al., 2018a).

846 The formation of the geodic textures in metre-scale pockets remains also questionable. The
847 mineralogical argument suggests that there are coeval with the vein system (this study). They do not
848 show any argument for structural control but they are clearly post–dating the massive mineralisation
849 based on cross-cutting relationships. Such an open space environment, as already suggested by
850 Ennaciri et al. (1997), is consistent with the transtensional character of the second mineralising event
851 as discussed above. Moreover, it can be suggested that the metre-scale pockets can finally re-use and
852 benefit from the high porosity and large open space that can exist in the slope-related breccia lenses
853 that served as a trap for the massive mineralisation. Such open spaces are represented in the schematic
854 petro-structural evolution of the deposit (Fig. 15).

855 Leblanc (1975) estimated the age of Bou Azzer mineralisation to be Neoproterozoic, based on
856 general arguments. Palaeozoic age was proposed by Essarraj et al. (2005) explaining that the Bou
857 Azzer district was formed by basinal brines circulation occurring during the early stage of the Atlantic
858 rifting. Inversely, Oberthür et al. (2009), that obtained Hercynian ages, proposed a possible reworking
859 of older minerals. Applying the indirect data obtained in this study and specifically the fact that both

860 types of mineralisation seem to develop in continuity (mineralogical arguments), it is strongly
861 suggested here that the Bou Azzer mineralisation was formed during the same period of time. The
862 tectonic context that prevailed during vein formation, defined by conjugate NS dextral and NE left-
863 lateral normal veins (Fig. 8), seems similar to the second transtension stage that has been defined and
864 demonstrated recently by Tuduri et al. (2018a) as a major tectonic event that affected the Jbel Saghro,
865 more to the N-NE (see above). In that case, the formation of earlier massive mineralisation could have
866 taken place only during the early Neoproterozoic, fact that is consistent with the intervention of
867 hyper-extension in response to the north-directed subduction suspected southward of the Bou Azzer
868 district (Triantafyllou et al., 2016).

869 With such a hypothesis, the numerous young ages obtained in this area could be related to
870 remobilisation processes during the Hercynian orogeny. In fact, the large spectrum of ages between
871 310 to 70 Ma presents an evidence of improper duress of dating, certainly in favour of unsatisfying
872 results. Because the Hercynian hypothesis is frequently advanced within the entire Anti-Atlas by a
873 number of authors (see discussion in Levresse et al., 2017) one can question about the numerous
874 geochronological data obtained within the entire Anti-Atlas (see also Essarraj et al., 2016) while no
875 structure can be clearly related to these Hercynian or maybe younger orogenesis. A recent article
876 underlined fault reactivation during Variscan and Alpine cycles but this appears no sufficient to
877 explain such an abundance of absolute ages. As the entire Anti-Atlas was buried under a thick marine
878 sedimentary cover from Middle Cambrian to Lower Devonian (Soulaimani et al., 2014), we question
879 if such a landfill can be at the origin of age rejuvenation and consequently of the numerous young
880 ages reported in this area (Caby, personal communication).

881

882 ## 6.5. Deposit classification and consequences for exploration strategy

883 The Bou Azzer district has been considered recently as a five-element veins type deposit by
884 Markl et al. (2016) and Burisch et al. (2017). The five-element veins deposits (Bi-Co-Ni-Ag±U) have
885 open-space infill characterised by two specific mineral associations: Co-Ni sulphides and Co-Ni
886 arsenides, with or without dendritic to wire-like texture of native elements like silver, arsenic and
887 bismuth in a carbonate gangue. They are related to hydrothermal processes affecting various
888 sedimentary, igneous or metamorphic rocks. Indeed, it is clear that deposits of the Bou Azzer district
889 and particularly the Ag-rich *Tizi* deposit (see location in Fig. 2) can be easily compared to the five-
890 element veins classification as already suggested. However, a lot of questions subsist. First, although
891 the late Ag-Hg stage clearly takes place after the Co-As and base metal stages (Leblanc and Lbouabi,
892 1988; Ennaciri et al., 1997; Essarraj et al., 2005), the age of their formation, the genetic link with the
893 Bou Azzer Co-Ni-As mineralisation and the mode of formation remain uncertain. Second, the five-
894 element veins classification does not provide a satisfying model of formation although a few genetic

895   theories have been proposed by Kissin (1992); one of them related to a magmatic-hydrothermal

896   concept occurring in the continental crust and associated with extensional tectonics. Indeed, this

897   unsatisfying situation justifies the new and original model of formation discussed above in this work.

898   Although the model of formation proposed in this study brings significant information regarding the

899   distribution and the characteristics of the numerous and various Ni-Co-As orebodies of the whole Bou

900   Azzer district, a large uncertainty subsists about the processes of metal concentration specifically for

901   the massive orebodies. Our study provides additional evidence that at least the massive part of the

902   mineralisation was formed by in-situ transformation of existing minerals such as spinel and magnetite.

903   We do not success in demonstrating if this transformation is dominated by replacement, overgrowth,

904   remobilisation or dissolution-precipitation process although recent studies favours replacement (e.g.,

905   Gervilla et al., 2012; Fanlo et al., 2015). The model of formation of the Bou Azzer deposits may

906   resemble to the replacement processes highlighted in some models of volcanic-hosted massive

907   sulphide (VHMS) formation (Aerden, 1993; Relvas et al., 2000; Doyle and Allen, 2003), except that

908   relationship with the main metamorphism event is not demonstrated at Bou Azzer. Gervilla et al.

909   (2012) mentioned it for the case of the Co-Ni-As Bou Azzer district. In spite of the nature of the Co-

910   Ni-As mineralisation and the lack of abundant polymetallic sulphides, we can tentatively suggest that

911   the Bou Azzer district may correspond to a model close to the one of the VHMS but with formation of

912   arsenides rather than sulphides. The drastic divergence between the two end-members, i.e. sulphide

913   versus arsenide, can be explained by the implication of the particular association between ultramafic

914   rocks (serpentinite) and plutonic (quartz diorite) in the second case, i.e., the Bou Azzer case. Indeed,

915   we propose that the Bou Azzer district is related to Massive Arsenide deposit instead of a Massive

916   Sulphide one. The term "Volcanic Hosted" can be replaced, in this case, by "Serpentinite Hosted" and

917   the acronym used could be SHMA, Serpentinite-Hosted Massive Arsenide. In this model, the

918   distribution of the previous breccia lenses is the most important factor in order to explain the

919   distribution of massive mineralisation ore bodies. This may explain why the Bou Azzer district is

920   composed of numerous, isolated, small-size, orebodies rather than a continuous and regular

921   mineralisation.

922

923   **7. Conclusion**

924   Based on new field, structural, textural, petro-structural and mineralogical arguments, we

925   propose a new genetic model for the famous Bou Azzer Co-Ni-As (-Au-Ag) district that explains the

926   formation of the two types of mineralisation. Because of the particular significance of the serpentine

927   and the original arsenide-rich mineralogy, we propose to call this type of deposit SHMA

928   (Serpentinite-Hosted Massive Arsenides). In this hypothesis, several lines of evidence argue for this

929   new classification. Because the massive part of the deposit is formed by circulation of hydrothermal

930   fluids across a serpentinite breccia formed during tectonic exhumation along low-angle extensional

931   detachment, the model of formation is similar to the one of VHMS except the fact that "basement and

932 source" rocks are serpentinite rather than volcanic or oceanic crust. The significance of replacement
933 processes is an additional argument for explaining their mode of formation. The presence of intrusive
934 rocks and exhumed mantle transformed to serpentinite (source for Ni and Co) is essential for the
935 formation of this deposit type. The nature of the low-angle extensional contact is not, for the moment,
936 entirely demonstrated. Preliminary observations (Fig. 3A) argue for general extensional setting
937 (Tourneur et al., 2019).

938

947

948

949 **References**
950 Admou, A., Razin, Ph., Egal, E., Youbi., N., Soulaimani, A., Blein, O., Chèvremont, Ph., Gasquet, D.,
951 Barbanson, L., Bouabdelli, M., Anzar-Conseil, 2013. Notice explicative, carte geol. Maroc
952 (1/50000). Notes et Mémoires Serv. Géol. Maroc N°533bis, MEM/BRGM.

953 Aerden, D.G.A.M., 1993. Formation of Massive Sulfide Lenses by Replacement of Folds: The
954 Hercules Pb-Zn Mine, Tasmania. Econ. Geol., 88, 377-396.

955 Ahmed A.H., Arai, S., Abdel-Aziz; Y.M., Rahimi, A., 2005. Spinel composition as a petrogenetic
956 indicator of the mantle section in the Neoproterozoic Bou Azzer ophiolite, Anti-Atlas,
957 Morocco. Precam. Res., 138, 225–234.

958 Ahmed, A.H., Arai, S., Ikenne, M., 2009. Mineralogy and paragenesis of the Co-Ni arsenides ores of
959 Bou Azzer, Anti-Atlas, Morocco. Econ. Geol., 104, 249-266.

960 Alt, J.C., 1995. Subseafloor processes in mid-ocean ridge hydrothermal systems. Seafloor
961 Hydrothermal Systems. Physical, Chemical, Biological, and Geological Interactions, pp. 85-
962 114

963 Alt, J.C., Laverne, C., Vanko, D.A., Tartarotti, P., Teagle, D.A., Bach, W., Zuleger, E., Erzinger, J.,
964 Honnorez, I., Pezard, P.A., 1996. Hydrothermal alteration of a section of upper oceanic crust in
965 the eastern equatorial Pacific: A synthesis of results from Site 504 (DSDP Legs 69, 70, and 83,
966 and ODP Legs 111, 137, 140, and 148). Proceedings of the Ocean Drilling Program: Scientific
967 Results, 148, 417-434.

968 Alt, J.C., Shanks, W., 1998. Sulfur in serpentinized oceanic peridotites: Serpentinization processes
969   and microbial sulfate reduction. J. Geophys. Res., 103, 9917–9929. doi:10.1029/98JB00576

970 Arndt, N.T., Lesher, C.M., Czamanske, G.K., 2005. Mantle-derived magmas and magmatic Ni-Cu-
971   (PGE) deposits, In: Hedenquist, J.W., Thompson, J.F.H., Goldfarb, R.J., Richard, J.P. (Eds.),
972   Economic Geology, 100th Anniversary Volume, pp. 5-23.

973 Barbey, P., Oberli, F., Burg, J.P., Nachit, H., Pons, J., Meier, M., 2004. The Paleoproterozoic in
974   western Anti-Atlas (Morocco): A clarification. J. African Earth Sci, 39, 239-245.

975 Bastin, E.S., 1939. The nickel-cobalt-native silver ore type. Econ. Geol., 34, 1-40.

976 Beraaouz, E. H., Ikenne, M., Mortaji, A., Madi, A., Lahmam, M., Gasquet, D., 2004. Neoproterozoic
977   granitoids associated with the Bou-Azzer ophiolitic melange (Anti-Atlas, Morocco): Evidence
978   of adakitic magmatism in an arc segment at the NW edge of the West-African craton. J. African
979   Earth Sci., 39, 285-293.

980 Blein, O., Baudin, T., Chèvremont, P., Soulaimani, A., Admou, H., Gasquet, P., Cocherie, A., Egal,
981   E., Youbi, N., Razin, P., Bouabdelli, M., Gombert, P., 2014. Geochronological constraints on
982   the polycyclic magmatism in the Bou Azzer-El Graara inlier (Central Anti-Atlas Morocco): J.
983   African Earth Sci., 99, 287-306.

984 Bodinier, J.L., Dupuy, C., Dostal, J., 1984. Geochemistry of Precambrian ophiolites from Bou Azzer,
985   Morocco. Contrib. Miner. Petrol., 87, 43-50.

986 Boillot, G., Recq, M., Winterer, E.L., Meyer, A.W., Applegate, J., Baltuck, M., Bergen, J.A., Comas,
987   M.C., Davies, T.A., Dunham, K., Evans, C.A., Girardeau, J., Goldberg, G., Haggerty, J., Jansa,
988   L.F., Johnson, J.A., Kasahara, J., Loreau, J.P., Luna-Sierra, E., Moullade, M., Ogg, J., Sarti, M.,
989   Thurow, J., Williamson, M., 1987. Tectonic denudation of the upper mantle along passive
990   margins: a model based on drilling results (ODP leg 103, western Galicia margin, Spain).
991   Tectonophysics, 132, 335-342.

992 Borisenko, A.S., Lebedev, V.I., Borovikov, A.A., Pavlova, G.G., Kalinin, Y.A., Nevol'ko, P.A.,
993   Kostin, A.V., 2014. Forming Conditions and Age of Native Silver Deposits in Anti-Atlas
994   (Morocco). Doklady Earth Sciences, 456, 663–666.

995 Bouchta, R., Boyer, F., Routhier, P., Saadi, M., Salem, M., 1977. L'aire cuprifère de l'Anti-Atlas
996   (Maroc) : Permanence et arêtes riches. C. R. Acad. Sc. Paris, 284, 503-506.

997 Bourque, H., Barbanson, L., Sizaret, S., Branquet, Y., Ramboz, C., 2014. Copper Mineralisation in
998   Adoudounian Cover of the Bou Azzer-El Graara (Anti Atlas, Morocco): Tectono-Stratigraphic
999   Controls. Mineral Resources in a Sustainable Word, 4, 1575–1578.

1000 Bousquet, R., El Mamoun, R., Saddiqi, O., Goffé, B., Möller, A., Madi, A., 2008. Mélanges and
1001   ophiolites during the Pan-African orogeny: the case of the Bou-Azzer ophiolite suite
1002   (Morocco). Geological Society, London, Special Publications, 297, 233-247.

1003 Burisch, M., Gerdes, A., Walter, B., Neumann, U., Fettel, M., Markl, G., 2017. Methane and the
1004   origin of five-element veins: Mineralogy, age, fluid inclusion chemistry and ore forming
1005   processes in the Odenwald, SW Germany. Ore Geol. Rev., 81, 42-61.

1006 Burkhard, M., Caritg, S., Helg, U., Robert-Charrue, C., Soulaimani, A., 2006. Tectonics of the Anti-
1007   Atlas of Morocco. C. R. Geosciences, 338, 11-24.

1008 Butt, C.R.M., Cluzel, D., 2013. Nickel Laterite Ore Deposits: Weathered Serpentinites. Elements, 9,
1009   123-128.

1010 Caby, R., 2014. Nature and evolution of Neoproterozoic ocean-continent transition: Evidence from
1011   the passive margin of the West African craton in NE Mali. J. African Earth Sci, 91, 1-11.

1012 Cailteux, J.L.H., Kampunzu, A.B., Lerouge, C., Kaputo, A.K., Milesi, J.P., 2005. Genesis of
1013   sediment-hosted stratiform copper–cobalt deposits, central African Copperbelt. J. African Earth
1014   Sci., 42, 134-158.

1015 Clerc, C., Lagabrielle, Y., Neumaier, M. Reynaud, J.Y., Saint Blanquat, M., 2012. Exhumation of
1016   subcontinental mantle rocks: evidence from ultramafic-bearing clastic deposits nearby the
1017   Lherz peridotite body, French pyrenees. Bull. Soc. Géol. Fr., 5, 443-459.

1018 Chauvet, A., Tourneur, E., Paquez, C., Bodinier, J.L., Ennaciri, A., in preparation. A new geodynamic
1019   vision of the Bou Azzer - El Graara inlier, Anti-Atlas, Morocco. Obduction versus hyper
1020   extension model. To be submitted in Journal of Structural Geology.

1021 Choubert, G., 1945. Sur le Précambrien marocain. C. R. Acad. Sci Paris, 221, 249-251.

1022 Choubert, G., 1963. Histoire géologique du Précambrien de l'Anti-Atlas. Notes Mem. Serv. Géol.
1023   Maroc, 162, 352 p.

1024 Choubert, G., Faure-Muret, A., 1980. Anti-atlas (Morocco). Earth-Science Reviews, 16, 87-113

1025 Clauer, N., 1976. Géochimie isotopique du strontium des milieux sédimentaires – application à la
1026   géochronologie de la couverture du craton Ouest-Africain. Sci. Géol. Mém., 45, 256 p.

1027 Coltat, R., Branquet, Y., Gautier, P., Campos Rodriguez, H., Poujol, M., Pelleter, E., McClenaghan,
1028   S., Manatschal, G. and Boulvais, P., 2019. Unravelling the root zone of ultramafic-hosted black
1029   smokers-like hydrothermalism from an Alpine analog. Terra Nova, 31(6), 549-561.

1030 Dolansky, L.M., 2007. Controls on the genesis of hydrothermal cobalt mineralisation: Insights from
1031   the mineralogy and geochemistry of the Bou Azzer deposits, Morocco. Unpublished M.Sc.
1032   thesis, Montreal, Canada, McGill University, 192 p.

1033 Downs, R.T., 2006. The RRUFF Project: an integrated study of the chemistry, crystallography,
1034   Raman and infrared spectroscopy of minerals. Program and Abstracts of the 19th General
1035   Meeting of the International Mineralogical Association in Kobe, Japan. O03-13.

1036 Doyle, M.G., Allen, R.L., 2003. Subsea-floor replacement in volcanic-hosted massive sulfide
1037   deposits. Ore Geol. Rev., 23, 183-222

1038 El Ghorfi, M., Oberthür, T., Lüders, V., El Boukhari, A., Melcher, F., Maacha, L., Ziadi, R.,
1039   Baoutoul, H., 2006. Gold–palladium mineralisation at Bleïda Far West, Bou Azzer–El Graara
1040   Inlier, Anti-Atlas, Morocco. Miner. Dep., 41, 549-564.

1041 El Hadi, H., Simancas, J.F., Martínez-Poyatos, D., Azor, A., Tahiri, A., Montero, P., Fanning, C.M.,
1042   Bea, F., González-Lodeiro, F., 2010. Structural and geochronological constraints on the
1043   evolution of the Bou Azzer Neoproterozoic ophiolite (Anti-Atlas, Morocco). Precam. Res., 182,
1044   1-14.

1045 Ennaciri, A., 1995. Contribution à l'étude du district à Co, As, (Ni, Au, Ag) de Bou Azzer, Anti-Atlas
1046   (Maroc). Données minéralogiques et géochimiques : Etude des inclusions fluides. Unpublished
1047   M.Sc. thesis, University of Orléans, 238 p.

1048 Ennaciri, A., Barhanson, L., Touray, J.C., 1995. Mineralised hydrothermal solution cavities in the Co-
1049   As Aït Ahmane mine (Bou Azzer, Morocco). Miner. Dep., 30, 75- 77.

1050 Ennaciri, A., Barbanson, L., Lancelot, J., Touray, J.C., 1996. Distribution et âge de mise en place des
1051   minéralisations aurifères du district de Bou Azzer) (Anti-Atlas, Maroc): Abstract, Réunion des
1052   Sciences de la Terre, 16th, Orléans, p. 153.

1053 Ennaciri, A., Barbanson, L., Touray, J. C., 1997. Brine inclusions from the Co-As(Au) Bou Azzer
1054   district, Anti-Atlas mountains, Morocco. Econ. Geol., 92, 360-367.

1055 Ennih, N., Liégeois, J., 2001. The Moroccan Anti-Atlas : the West African craton passive margin with
1056   limited Pan-African activity. Implications for the northern limit of the craton. Precam. Res.,
1057   112, 289–302.

1058 Essarraj, S., Boiron, M.C., Cathelineau, M., Banks, D.A., Benharref, M., 2005. Penetration of surface-
1059   evaporated brines into the Proterozoic basement and deposition of Co and Ag at Bou Azzer
1060   (Morocco): Evidence from fluid inclusions. J. African Earth Sci, 41, 25-39.

1061 Essarraj, S., Boiron, M.C., Cathelineau, M., Tarantola, A., Leisen, M., Boulvais, P., Maacha, L., 2016.
1062   Basinal brines at the origin of the Imiter Ag-Hg deposit (Anti-Atlas, Morocco): Evidence from
1063   LA-ICP-MS data on fluid inclusions, halogen signatures, and stable isotopes (H, C, O). Econ.
1064   Geol., 111, 1753-1781.

1065 Fanlo, I., Gervilla, F., Colás, V., Subías, I., 2015. Zn-, Mn- and Co-rich chromian spinels from the
1066   Bou-Azzer mining district (Morocco): Constraints on their relationship with the mineralising
1067   process. Ore Geol. Rev., 71, 82–98. https://doi.org/10.1016/j.oregeorev.2015.05.006

1068 Freyssinet, P., Butt, C.R.M., Morris, R.C., Piantone, P., 2005. Ore-forming processes related to
1069   lateritic weathering. In: Hedenquist, J.W., Thompson, J.F.H., Goldfarb, R.J., Richard, J.P.
1070   (Eds.), Economic Geology 100th Anniversary Volume. Society of Economic Geologists, Inc,
1071   Littleton, Colourado, pp. 681-722.

1072 Gahlan, H., Arai, S., Ahmed, A.H., Ishida, Y., Abdel-Aziz, Y.M., Rahimi, A., 2006. Origin of
1073   magnetite veins in serpentinite from the Late Protero- zoic Bou-Azzer ophiolite, Anti-Atlas,

1074   Morocco: An implication for mobility of iron during serpentinisation. J. African Earth Sci., 46,
1075   318–330.

1076   Gasquet, D., Levresse, G., Cheilletz, A., Azizi-Samir, M.R., Mouttaqi, A., 2005. Contribution to a
1077   geodynamic reconstruction of the Anti-Atlas (Morocco) during Pan-African times with the
1078   emphasis on inversion tectonics and metallogenic activity at the Precambrian-Cambrian
1079   transition. Precam. Res., 140, 157-182.

1080   Gervilla, F., Fanlo, I., Colas, V., Subias, I., 2012. Mineral composition and phases relation of Ni – Co
1081   – Fe arsenides ores from the Aghbar mine, Bou Azzer, Morocco. The Canadian Mineralogist,
1082   50, 447-470.

1083   Hajar, Z., Gervilla, F., Fanlo, I., Jiménez, J.M.G., Ilmen, S., 2020, Formation of serpentinite-hosted,
1084   Fe-rich arsenide ores at the latest stage of mineralization of the Bou-Azzer mining district
1085   (Morocco). Ore Geol. Rev. In Press.

1086   Hattori, K., Takahashi, Y., Guillot, S., Johanson, B., 2005. Occurrence of arsenic (V) in forearc
1087   mantle serpentinites based on X-ray absorption spectroscopy study. Geochim. Cosmoschim.
1088   Acta, 69, 5585-5596

1089   Hefferan, K.P., Admou, H., Karson, J.A., Saquaque, A., 2000. Anti-Atlas (Morocco) role in
1090   Neoproterozoic Western Gondwana reconstruction. Precam. Res., 103, 89-96.

1091   Hein, J.R., Koschinsky, A., 2014. Deep-Ocean Ferromanganese Crusts and Nodules. In: Holland,
1092   H.D., Turekian, K.K. (Eds.), Treatise on Geochemistry (Second Edition), volume 13, chapter
1093   11, Elsevier, Oxford, pp. 273-291.

1094   Hitzman, M.W., Broughton, D., Selley, D., Woodhead, J., Wood, D., Bull, S., 2012. The Central
1095   African Copperbelt: Diverse stratigraphic, structural, and temporal settings in the world's
1096   largest sedimentary copper district. In: Hedenquist, J.W., Harris, M., Camus, F. (Eds.), Geology
1097   and Genesis of Major Copper Deposits and Districts of the World: A Tribute to Richard H.
1098   Sillitoe. Society of Economic Geologists, Littleton, Co, pp. 487-514.

1099   Hollard, H., Choubert, G., Bronner, G., Marchand, J., Sougy, J., 1985. Carte géologique du Maroc,
1100   échelle: 1/1.000.000. Notes et Mémoires du Service Géologique du Maroc, 260 p.

1101   Hölker, A., Manatschal. G., Holliger, K., Bernoulli, D., 2003. Tectonic nature and seismic response of
1102   top-basement det achment faults in magma-poor rifted margins. Tectonics, 22, 4, 1035.

1103   Ikenne, M., Madi, A., Gasquet, D., Cheilletz, A., Hilal, R., Mortaji, A., Mhaili, E., 2005. Petrogenetic
1104   significance of podiform chromitites from the Neoproterozoic ophiolitic complex of Bou Azzer
1105   (Anti-Atlas, Morocco). Africa Geosci. Rev., 12 (2), 131-143.

1106   Ikenne, M., Souhassou, M., Saintilan, N.J., Karfal, A., El Hassani, A., Moundi, Y., Ousbih, M.,
1107   Ezzghoudi, M., Zouhir, M., Maacha, L., 2020. Cobalt-Nickel-Copper arsenide, sulpharsenide
1108   and sulphide mineralisation in the Bou Azzer window, Anti-Atlas, Morocco: One century of
1109   multi-disciplinary and geological investigations, mineral exploration and mining. Geological
1110   Society, London, Special Publications, 502. https://doi.org/10.1144/SP502=2019-132

1111 Inglis, J.D., Lemos, R.S.D., Samson, S.D., Admou, H., 2005. Geochronological Constraints on Late
1112   Precambrian Intrusion, Metamorphism and Tectonism in the Anti-Atlas Mountains. The Journal
1113   of Geol., 113, 439-450.

1114 Ishii, T., Robinson, P.T., Maekawa, H., Fiske, R., 1992. Petrological studies of peridotites from
1115   diapiric serpentinite seamounts in the Izu–Ogasawara–Mariana Forearc, Leg 125. In: Fryer, P.,
1116   Pearce, J.A., Stokking, L.B., et al. (Eds.), Proceeding of the Ocean Drilling Program, Scientific
1117   Results, 125, 445-485.

1118 Jolivet, L., Menant, A., Clerc, C., Sternai, P., Bellahsen, N., Leroy, S., Pik, R., Stab, M., Faccenna, C.,
1119   Gorini, C., 2018. Extensional crustal tectonics and crust-mantle coupling, a view from the
1120   geological record. Earth-Science Rev., 185, 1187-1209.

1121 Kissin, S.A., 1992. Five-element (Ni-Co-As-Ag-Bi) veins: Geosciences Canada, 19, 113-124.

1122 Kreissl, S., Gerdes, A., Walter, B., Neumann, U., Wenzel, T., Markl, G., 2018. Reconstruction of a >
1123   200 Ma multi-stage "five-element" Bi-Co-Ni-Fe-As-S system in the Pennininc Alps,
1124   Switzerland. Ore Geol. Rev., 95, 746-788.

1125 Lagabrielle, Y., Bodinier, J.L., 2008. Submarine reworking of exhumed subcontinental mantle rocks:
1126   Field evidence from the Lherz peridotites, French Pyrenees. Terra Nova, 20, 11-21.
1127   https://doi.org/10.1111/j.1365-3121.2007.00781.x

1128 Latham, A.J., Riding, R., 1990. Fossil evidence for the location of the Precambrian-Cambrian
1129   boundary in Morocco. Nature, 344, 752–754.

1130 Laubier, M., Grove, T.L., Langmuir, C.H., 2014. Trace element mineral/melt partitioning for basaltic
1131   and basaltic andesitic melts: An experimental and laser ICP-MS study with application to the
1132   oxidation state of mantle source regions. Earth Planet. Sci. Lett., 392, 265-278.

1133 Leblanc, M., 1975, Ophiolites précambriennes et gîtes arseniés de cobalt (Bou Azzer, Maroc).
1134   Unpublished M.Sc. thesis, University of Montpellier, 329 p.

1135 Leblanc, M., 1976. Proterozoic oceanic crust at Bou Azzer. Nature, 261, 34-35.

1136 Leblanc, M., 1981. The Late Proterozoic ophiolites of Bou Azzer (Morocco): evidence for Pan-
1137   African plate tectonics. In: A. Kröner (Editor), Precambrian Plate Tectonics. Elsevier,
1138   Amsterdam, pp. 435-451.

1139 Leblanc, M., Billaud, P., 1982. Cobalt arsenide orebodies related to an upper Proterozoic ophiolite:
1140   Bou Azzer (Morocco). Econ. Geol., 77, 162-175.

1141 Leblanc, M., and Fischer, W., 1990. Gold and platinum group elements in cobalt arsenide ores:
1142   Hydrothermal concentration from a serpentinite source-rock. Mineralogy and Petrology, 42,
1143   197-209.

1144 Leblanc, M., Lbouabi, M., 1988. Native Silver Mineralisation along a Rodingite Tectonic Contact
1145   between Serpentinite and Quartz Diorite (Bou Azzer, Morocco). Econ. Geol., 83, 1379-1391.

1146 Levresse, G., 2001. Contribution à l'établissement d'un modèle génétique des gisements d'Imiter
1147   (Ag-Hg), Bou Madine (Pb-Zn-Cu-Ag-Au) et Bou Azzer (Co-Ni-As-Ag-Au) dans l'Anti-Atlas
1148   marocain. Unpublished M.Sc. thesis, CRPG-CNRS, Nancy, France, 191 p.

1149 Levresse, G. Bouabdellah, M., Gasquet, D., Cheilletz, A., 2017. Basinal brines at the origin of the
1150   Imiter Ag-Hg deposit (Anti-Atlas, Morocco): Evidence froim LA-ICP-MS data on fluid
1151   inclusions, Halogen signatures, and stable isotopes (H, C, O) – A discussion. Econ. Geol., 112,
1152   1269-1277.

1153 Maacha, L., Alansari, A., Saquaque, A., Soulaimani, A., 2012. The Bou Azzer Cobalt-Nickel-Arsenic
1154   District. In: Les principales mines du Maroc, Michard, A., Saddiqi, O., Chalouan, A., Rjimati,
1155   C., Mouttaqi, A. (Eds.). Nouveaux Guides Géologiques et Miniers du Maroc, pp. 91-97.

1156 Maacha, L., Elghorfi, M., Ennaciri , A., Sadiqqi, O., Soulaimani, A., Alansari, A., Bhilisse, M., 2015.
1157   Nouvelles données isotopiques et d'inclusions fluides des minéralisations cobaltifères de Bou
1158   Azzer. Apport à la géologie économique de la boutonnière. (Anti-Atlas central, Maroc). Notes
1159   et Memoires du service Géologique, 579, 133-139.

1160 Manatschal, G., 2004. New models for evolution of magma-poor rifted margins based on a review of
1161   data and concepts from West Iberia and the Alps. Intern. J. Earth Sci., 93, 432-466.
1162   https://doi.org/10.1007/s00531-004-0394-7

1163 Manatschal, G., Engström, A., Desmurs, L., Schaltegger, U., Cosca, M., Müntener, O., Bernoulli, D.,
1164   2006. What is the tectono-metamorphic evolution of continental break-up: The example of the
1165   Tasna Ocean–Continent Transition. J. Struct. Geol., 28, 1849-1869.

1166 Manheim, F.T., Lane-Bostwick, C.M., 1988. Cobalt in ferromanganese crusts as a monitor of
1167   hydrothermal discharge on the Pacific sea floor. Nature, 335, 59-62.

1168 Markl, G., Burisch, M., Neumann, U., 2016. Natural fracking and the genesis of five-element veins.
1169   Miner. Dep., 51, 703–712.

1170 Mifdal, A., Peucat, J.J., 1985. U-Pb and Rb-Sr dating of acidic volcanic rocks and Precambrian
1171   basement in Anti-Atlas of Morocco (Ouarzazate). Contribution for numerical dating of
1172   Precambrian-Cambrian boundary. Sciences Géologiques, Bulletins et Mémoires, 38, 185-200.

1173 Missenard, Y., Zeyen, H., Frizon de Lamotte, D., Leturmy, P., Petit, C., Sébrier, M., Saddiqi, O.,
1174   2006. Crustal versus asthenospheric origin of relief of the Atlas Mountains of Morocco. J.
1175   Geophys. Res.- Solid Earth, 111, B03401.

1176 Naldrett, A.J., 2005. A history of our understanding of magmatic Ni-Cu sulfide deposits. Can.
1177   Mineral., 43, 2069-2098.

1178 Oberthür, T., Melcher, F., Henjes-Kunst, F., Gerdes, A., Stein, H., Zimmerman, A., El Ghorfi, M.,
1179   2009. Hercynian age of the Cobalt-Nickel-Arsenide-(Gold) ores, Bou Azzer, Anti-Atlas,
1180   Morocco, Re-Os, Sm-Nd, and U-Pb age determinations. Econ. Geol., 104, 1065-1079.

1181 Pirrie, D., Butcher, A.R., Power, M.R., Gottlieb, P., Miller, G.L., 2004. Rapid quantitative mineral
1182   and phase analysis using automated scanning electron microscopy (QEMSCAN); potential

1183 applications in forensic geoscience. Geological Society, London, Special Publication, 232, 123-
1184 136.

1185 Pouit, G., 1966. Paléogéographie et répartition des minéralisations stratiformes de cuivre dans l'anti-
1186 Atlas occidental (Maroc). Chron Rech Min, 356, 279-289.

1187 Relvas, J., 2000. Geology and metallogenesis at the Neves Corvo deposit. Unpublished M.Sc. Thesis,
1188 Universidade de Lisboa, Portugal. 319 p.

1189 Richardson, C.J., Cann, J.R., Richards, H.G., Cowan, J.G., 1987. Metal-depleted root zones of the
1190 Troodos ore-forming hydrothermal systems, Cyprus. Earth Planet. Sci. Let., 84, 243-253.

1191 Samson, S. D., Inglis, J. D., D'Lemos, R. S., Admou, H., Blichert-Toft, J., Hefferan, K., 2004.
1192 Geochronological, geochemical, and Nd-Hf isotopic constraints on the origin of Neoproterozoic
1193 plagiogranites in the Tasriwine ophiolite, Anti-Atlas orogen, Morocco. Precam. Res., 135, 133-
1194 147.

1195 Saquaque, A., Admou, H., Karson, J., Hefferan, K., Reuber, I., 1989. Precambrian accretionary
1196 tectonics in the Bou Azzer-El Graara region, Anti-Atlas, Morocco. Geology, 17, 1107-1110.

1197 Smedley, P.L., Kinniburgh, D.G., 2002. A review of the source, behaviour and distribution of arsenic.
1198 Natural waters, 17, 517-568.

1199 Soulaimani, A., Michard, A., Ouanaimi, H., Baidder, L., Raddi, Y., Saddiqi, O., Rjimati, E.C., 2014.
1200 Late Ediacaran-Cambrian structures and their reactivation during the Variscan and Alpine
1201 cycles in the Anti-Atlas (Morocco). J. African Earth Sci., 98, 1-19.
1202 https://doi.org/10.1016/j.jafrearsci.2014.04.025

1203 Thiéblemont, D., Chêne, F., Liégeois, J.P., Ouabadi, A., Le Gall, B., Maury, R.C., Jalludin, M.,
1204 Ouattara Gbélé, C., Tchaméni, R., Fernandez-Alonso, M., 2016. Geological Map of Africa at
1205 1:10 Million Scale, 35th International Geology Congress ed; CCGM-BRGM: Orléans, France.

1206 Thomas, R.J., Fekkak, A., Ennih, N., Errami, E., Loughlin, S.C., Gresse, P.G., Chevallier, L.P.,
1207 Liégeois, J.P., 2004. A new lithostratigraphic framework for the Anti-Atlas Orogen, Morocco.
1208 J. African Earth Sci., 39, 217-226.

1209 Tourneur, E., 2019. Circulation de fluides aux abords de failles d'échelle crustale : contraintes
1210 structurales, microtectoniques, inclusions fluides et géochimiques sur les processus de
1211 formation du gisement de Bou Azzer (Ni-Co), Anti-Atlas, Maroc. Sciences de la Terre.
1212 Université Montpellier, 377 p.

1213 Tourneur, E., Chauvet, A., Kouzmanov, K., Tuduri, J. Sizaret, S., 2019. Textural and mineralogical
1214 constraints on the mode of formation of the Bou Azzer Co-Ni arsenide mineralization (Anti-
1215 Atlas, Morocco): Tectonic implications. Proceeding of the 15th SGA biennial Meeting, 1, 17-20.

1216 Triantafyllou, A., Berger, J., Baele, J., Diot, H., Ennih, N., Plissart, G., Monnier, C., Watlet, A.,
1217 Bruguier, O., Spagna, P., Vandycke, S., 2016. The Tachakoucht - Iriri - Tourtit arc complex
1218 (Moroccan Anti-Atlas): Neoproterozoic records of polyphased subduction-accretion dynamics
1219 during the Pan-African orogeny. J. Geod., 96, 81-103.

1220 Triantafyllou, A., Berger, J., Baele, J.M., Bruguier, O., Diot, H., Ennih, N., Monnier, C., Plissart, G.,
1221   Vandycke, S., Watlet, A., 2018. Intra-oceanic arc growth driven by magmatic and tectonic
1222   processes recorded in the Neoproterozoic Bougmane arc complex (Anti-Atlas, Morocco).
1223   Precam. Res., 304, 39-63. https://doi.org/10.1016/j.precamres.2017.10.022

1224 Tucker, M.E., 1986. Carbon isotope excursions on Precambrian/Cambrian boundary beds, Morocco.
1225   Nature, 319, 48-50.

1226 Tuduri, J., 2005. Processus de formation et relations spatio-temporelles des minéralisations à or et
1227   argent en contexte volcanique Précambrien (Jbel Saghro, Anti-Atlas, Maroc). Unpublished
1228   M.Sc. thesis, CNRS, Orleans, France, University of Orleans, 468 p.

1229 Tuduri, J., Chauvet, A., Barbanson, L., Bourdier, J.L., Labriki, M., Ennaciri, A., Badra, L., Dubois,
1230   M., Ennaciri-Leloix, C., Sizaret, S., Maacha, L., 2018a. The Jbel Saghro Au(–Ag, Cu) and Ag–
1231   Hg Metallogenetic Province: Product of a Long-Lived Ediacaran Tectono-Magmatic Evolution
1232   in the Moroccan Anti-Atlas. Minerals, 8, 592.

1233 Tuduri, J., Chauvet, A., Barbanson, L., Labriki, M., Dubois, M., Trapy, P.H., Lahfid, A., Poujol, M.,
1234   Melleton, J., Badra, L., Ennaciri, A., Maacha, L., 2018b. Structural control, magmatic-
1235   hydrothermal evolution and formation of hornfels-hosted, intrusion-related gold deposits:
1236   Insight from the Thaghassa deposit in Eastern Anti-Atlas, Morocco. Ore Geol. Rev., 97, 171-
1237   198.

1238 Wafik, A., Admou, H., Saquaque, A., El Boukhari, A., Juteau, T., 2001. Cu-Fe sulfureous
1239   mineralisations and the associated alterations in the Bou Azzer and Khzama Proterozoic
1240   ophiolites, Anti-Atlas, Morocco. Ofioliti, 26, 47-62.

1241 Walsh, G.J., Benziane, F., Aleinikoff, J.N., Harrison, R.W., Yazidi, A., Burton, W.C., Quick, J.E.,
1242   Saadane, A., 2012. Neoproterozoic tectonic evolution of the Jebel Saghro and Bou Azzer-El
1243   Graara inliers, eastern and central Anti-Atlas, Morocco. Precam. Res., 216, 23-62.

1244

1245 **Figures Captions**

1246

1247 Figure 1: Localisation of the studied area at (A) the West African Craton scale (after Thiéblemont et
1248   al., 2016) and (B) at the Moroccan Anti-Atlas scale (after Hollard et al., 1985; Tuduri et al.,
1249   2018a). Different inliers are: AM: Agadir-Melloul; BD: Bas Drâa; If: Ifni; Ig: Iguerda; Im:
1250   Igherm; K: Kerdous; TA: Tagragra of Akka; TT: Tagragra de Tata; Z: Zenaga. C) Geological
1251   map of the Bou Azzer district modified after Leblanc (1975) and Admou et al. (2013).

1252

1253 Figure 2: Simplified block diagram showing the distribution of the main geological units of the Co-
1254   Ni-As (-Au-Ag) Bou Azzer district and also the main ore deposits studied in this study. All the
1255   underground occurrences here studied were indicated with depth level. See text for explanation.

1256

1257 Figure 3: Photographs of host rocks. A) Faulted contact with normal motion between serpentinite and
1258   carbonated complex shell (*Ambed* location, see Fig. 2). B) Intrusive contact of quartz diorite in
1259   mafic rocks (*Taghouni* location). C) Massive serpentinite with layers of magnetite, talc- and
1260   carbonate-alteration and stereonet diagram of the serpentinite cleavage pole (Schmidt stereonet,
1261   lower hemisphere, *Taghouni* location). D) Contact with rodingite between serpentinite and
1262   quartz diorite (*Taghouni,* level 80). E) Linear contact between serpentinite and quartz diorite
1263   showing the development of alteration halo in both rocks (*BAE P3* location).

1264

1265 Figure 4: Photographs of surface structures. A) *Bou Azzer East* field zone showing the contact
1266   between serpentinite, siliceous complex shell, mafic rock and quartz diorite. The siliceous
1267   gangue is affected by carbonate-rich large-scale pocket (white line) and contains serpentinite
1268   fragments (green line). B) Large-scale pull-apart structure composed of a siliceous gangue and
1269   exhibiting massive and/or laminated texture (zoom in the red square). C) *Filon 7* aspect at
1270   surface after it junction with the *Filon 5*. D) Large view of the *Bou Azzer Centre* mine showing
1271   the *Filon 7* extension reaching several hundred metres long. E) *Quarry 52* image representing
1272   veins cutting the massive mineralisation and serpentinite.

1273

1274 Figure 5: Macroscopic aspect of the massive mineralisation and veins in underground galleries. A)
1275   Typical Co-Ni-Fe bearing massive mineralisation separating serpentinite and carbonated
1276   gangue (*Aghbar*, level 410). B) Similar massive mineralisation against siliceous gangue (*Bou
1277   Azzer East P6*, level 510). C) Veins showing brecciated texture (with diorite fragments mainly)
1278   and composed of Co-Fe bearing minerals and late euhedral calcite pocket (Cal) (*Bou Azzer East
1279   P3*, level 80). D) Mineralised pockets composed of quartz/chlorite/skutterudite border, followed
1280   by comb-quartz and Co-Fe arsenides. Late rhombohedral calcite with fragments of Co-Fe
1281   arsenide is visible in the centre of the pockets (*Filon 53*, level 240).

1282

1283 Figure 6: A) 3D sketch of mineralised contact on surface and in gallery for comparison. B) Stereonet
1284   poles contour diagram of the massive mineralisation and the veins measured orientation on the
1285   field and galleries (Schmidt stereonet, lower hemisphere).

1286

1287 Figure 7: Photographs of vein structures in mining galleries. A and B are photographs of the vertical
1288   plane. C and D are photographs and corresponding sketch (D) of horizontal plane (view realised
1289   towards the top of the mining gallery). A) Normal vein structure illustrated by the offset of the
1290   epidote-rich vein (Ep-Vein) (*Filon 53*, level 240). B) Similar motion showing by pull-apart
1291   structure (Same area, *Filon 53*, level 240). C) Mineralised vein trending east and showing
1292   dextral motion (*Bouismas area*, level 390). D) Mineralised vein trending north-east and
1293   showing left-lateral motion with interpretative sketch (*Bou Azzer East, Puit 3*, level 510).

1294

1295   Figure 8: Schematic diagram explaining the conjugate character of the vein system at Bou Azzer.
1296   Conjugate veins in the horizontal planes A systematic normal motions is observed in the
1297   vertical plane whereas NS and N070°E veins are dextral and sinistral, respectively, allowing to
1298   define a transtensional tectonic regime with a roughly NNE/SSW shortening direction.

1299

1300   Figure 9: Paragenetic sequence, texture and relative proportions of major elements (metals and
1301   sulphur) in the different structures of the Bou Azzer Co-Ni-As(-Au-Ag) district. Grey colour
1302   represents minerals of surrounding rocks, purple: Ni-stage, green; Co-stage, black: gangue
1303   minerals, blue: sulphide stage, orange: sodic-calcic alteration and pink: supergene alteration.
1304   (Ab: Albite, Adu: Adularia, As: Arsenic, Apy: Arsenopyrite, Bn: Bornite, Cal: Calcite, Cct:
1305   Chalcocite, Chl: Chlorite, Co: cobalt, Cob: Cobaltite, Ccp: Chalcopyrite, Dg: Digenite, Dol:
1306   Dolomite, Ep: Epidote, Ert: Erythrine, Fe: iron, Gd: Gersdorffite, Gn: Galena, K: potassium,
1307   Lo: Loellingite, Ni: nickel, Nk: Nickeline, Qz: Quartz, Ram: Rammelsbergite, S: Sulphide, Saf:
1308   Safflorite, Sku: Skutterudite, Sp: Sphalerite, Ttn: Titanite, Tlc: Talc, Tnt-Ttr: Tennantite -
1309   Tetrahedrite)

1310

1311   Figure 10: Mineral assemblages of the Ni-Co arsenide mineralisation at Bou Azzer. A) Quartz diorite
1312   composed of albite (Ab), quartz (Qz) and loellingite (Lo1) cross-cut by potassic feldspar (k-
1313   Fsp) (optical cathodoluminescence image, CL); B) Aspect of the serpentinite near massive
1314   mineralisation showing spinel (Spl) grain which is sometimes entirely replaced/transformed by
1315   rammelsbergite (see rectangle and zoom in Fig. 10C). Within the massive body, skutterudite is
1316   also fractured and fill by serpentinite (polarised light, PL); C) Isolated nuclei of rammelsbergite
1317   inside the serpentinite showing fracture filled by neoformed elongated serpentine (RL image).
1318   D) Laminated Massive Mineralisation (LMM) showing Ni-Co rich arsenide bands (nickeline,
1319   rammelsbergite, skutterudite, cobaltite) alternating with bands of calcite large crystal (Cal1) and
1320   sphalerite (RL). E) Disseminated spinel with magnetite-rich margin surrounded by
1321   rammelsbergite (Ram) and nickeline (Nk1) grains. F) Feathery rammelsbergite fragment (Ram)
1322   encapsulated inside successive crystallisation of skutterudite (Sku1), calcite (Cal1), infilling
1323   chalcopyrite (Ccp) and prismatic to cloudy loellingite (Lo1) ending by a massive gangue of
1324   euhedral banded skutterudite (Sku2) and calcite (Cal2) (RL image). G) RL image illustrating
1325   the brecciated character of the massive mineralisation (BMM) with rammelsbergite fragments
1326   surviving in core of a cobaltite (Cob1) - skutterudite (Sku2) - calcite (Cal1) - chalcopyrite (Ccp)
1327   matrix. Late calcite (Cal2) fills the interstitial open-space. H) Growing of star-shaped safflorite
1328   (Saf1) on rammelsbergite (not visible on the photography), followed by loellingite (Lo2) and
1329   large carbonate grain of the carbonated gangue (Cal2) (RL image, polarised).

1330

1331   Figure 11: Automated mineralogy: A) QEMSCAN mineral map of serpentinite in contact with the

1332   massive mineralisation at *Aghbar*. A strong talc alteration is observed in the left part of the

1333   sample (serpentinite) whereas a calcite impregnation is dominant in its right part (carbonated

1334   gangue of the mineralisation). Small (<2000 μm) spinel grains are preserved in the serpentinite

1335   whereas while they are replaced by large bornite grains, associated with skutterudite in the

1336   carbonate gangue. Cobaltite is disseminated in both part of the sample. B) QEMSCAN mineral

1337   map of the massive mineralisation at *Filon 53* composed mainly of very elongated

1338   rammelsbergite noddles surrounded by large skutterudite. Noddle distribution suggests that

1339   they were formed by replacement/transformation of initial fragments, possibly spinel grains

1340   (see text for explanation). Note that earlier carbonate can develop in contact with

1341   rammelsbergite and the final appearance of Cu-rich sulphides (i.e., chalcopyrite). C)

1342   QEMSCAN mineral map, Co and Ni element distribution maps for massive mineralisation at

1343   *Bouismass*. Skutterudite and rammelsbergite form zoned aggregates with successive Ni-rich

1344   and Co-rich growth zones. See text for explanation. Note that rammelsbergite forms isolated

1345   nucleus systematically surrounded by cobaltite and skutterudite. D) Transmitted-light image

1346   and QEMSCAN mineral map of vein structure at *Aghbar* showing textural relationship between

1347   skutterudite, spinel (chromite) and chlorite within a siliceous gangue. The Co map shows that

1348   skutterudite has Co-rich border. Note the late dolomite infill (sky blue colour on the

1349   QEMSCAN map). E) Transmitted-light image, QEMSCAN mineral map, Co and Ni element

1350   distribution maps from *Filon 7/5* vein structure. Small skutterudites (black arrow) are

1351   associated with the early dolomite grains and show not detectable Ni content. Inversely,

1352   cobaltite related to comb-quartz has significant Ni proportion. F) QEMSCAN mineral map and

1353   Co and Fe element distribution maps of a border of a vein structure (*Bouismass*), focused on

1354   skutterudite-loellingite relationship. Skutterudite is elongated, fractured and Co/Ni growth

1355   bands are less marked than in skutterudite from the massive mineralisation. Loellingite

1356   appearance is indicator of a Co/Fe transition.

1357

1358   Figure 12: Chemical composition of mineralisation from the serpentinite, the massive mineralisation,

1359   the vein system, the pockets and complex shells of the Bou Azzer area. A) As versus S (apfu)

1360   within different skutterudites. B) Fe+Ni versus Co (apfu) composition within skutterudite of the

1361   different type of deposits. C) Mg-Fe-Mn distribution within calcites (apfu). Data provide from

1362   EPMA analysis in Tourneur (2019).

1363

1364   Figure 13: Thin section illustrations of the carbonated mineralised gangue of the massive system and

1365   vein. A) Cobaltite (Cob2) and nickeline (Nk2) formed along fractures inside rammelsbergite

1366   minerals (RL image). Note the occurrence of late calcite (Cal4). B) Optical-CL image of a

1367   spinel (Spl) grain partially replaced by the carbonated gangue from the massive mineralisation.

A magnetite-rich margin (Mag) was identified and confirmed by EPMA. C) Laminated nickeline (Nk1) surrounded by skutterudite (Sku2) synchronous with calcite (Cal1) as demonstrated by successive and alternating growth bands (massive mineralisation, RL image). D) Skutterudite associated with dolomite (Dol1) and comb quartz in veins. Cobaltite (Cob2) is supposed to form during a second stage between comb quartz (Qz2) and by replacement of skutterudite (Sku3); E) Adularia (Adu) with a triangular shape forming along vein margin. Minerals inside the vein are quartz (Qz3) and calcite (Cal3) whereas adularia growth on albite mineral of the surrounding rock (Ab) (PL image). F) Rim of a geodic pocket texture exhibiting loellingite (Lo2) and cobaltite (Cob3) (Co-Fe arsenide in the picture) large minerals followed by comb quartz (Qz3) and large calcite (Cal3-4) crystallisation (RL image, polarised). G) Cold-CL image of carbonated gangue showing the brecciated aspect with earlier calcite fragment (Cal2) and the late crystallisation of euhedral large calcite grains (Cal2). H) Serpentinite fragments in the carbonated gangue (Cal2) (PL image).

Figure 14: Additional textural observations. A) High magnification view of the red rectangle area indicated of the Figure 11B. Note that detailed texture of rammelsbergite grains show the existence of two generations: a first mineral formed the elongated grains and some second acicular crystals with higher Co values overgrown on them. This texture indicates rapid crystallisation under oversaturated conditions. B) Cold-CL image of calcite gangue of massive mineralisation showing the occurrence of previous ghost mesh textures now entirely transformed in calcite minerals (see the interpretative sketch). C) BSE image of serpentinite where the texture could be transformed by carbonation in order to form the ghost mesh texture of the Figure 14B.

Figure 15: Interpretative three-stage petro-structural model of the Bou Azzer Co-Ni mineralisation formation. All indications in red within this figure are interpretations whereas the ones in black are observations. A and A1) Pre-mineralisation stage showing the significant role of the existence of elongated lenses of serpentinite breccia at the contact between serpentinite and quartz diorite. Note the presence of spinel minerals, magnetite layers (future Ni-rich minerals) and open space (future mineralised pockets). B) In situ formation of the massive mineralisation by percolation, leaching, replacement, transformation of the brecciated lenses (see text for details). Two stages were identified, a Ni-Co-As one with formation of nickeline and rammelsbergite (B1) and a Co-As-Fe-S stage with crystallisation of skutterudite and cobaltite forming massive bodies and associated to the formation of carbonated and/or siliceous gangue (B2). Fragments of serpentinite were still visible in the gangue. C and C1) Vein formation stage under the control of NNNE-SSW transtensional tectonic event. Co-rich minerals formed followed by the general emplacement of late Fe-S minerals (sulphide stage).

1405

1406 Figure 16: Hypothetic tectonic context favourable for the formation of the mineralisation system of

1407 the Bou Azzer district (Morocco). Normal fault was supposed to develop zone of tectonic

1408 breccia and mylonitic deformational zones that will serve as trap for the future massive

1409 mineralisation. In such a scenario, fault motion is considered as normal (see text for

1410 explanation) and Brecciated Massive Mineralisation (BMM) were formed in brecciated lenses

1411 whereas Laminated Massive Mineralisation (LMM) developed in previously-formed mylonitic

1412 zone. Note the frequent occurrence of mafic rocks at the limit between the serpentinite and the

1413 intrusive quartz diorite.

1414

1415 Table 1: Information on the different locations analysed in this study: sampling depths, coordinates of

1416 wells in WGS84, mineralisation type are indicated.

1417 Highlights

1418 • Two types of mineralisation characterised the Bou Azzer District
1419 • Massive mineralisations are forming by remobilisation processes from relics of spinels
1420 • Veins system are linked with a mode of formation associated with tectonics
1421 • Continuous evolution from Ni-rich to Co-rich mineralisations in all structures
1422 • The mineralised bodies correspond to ancient sedimentary breccia
1423 • The mineralised bodies are formed in slope of detachement faults that allow to exhume
1424 mantle rocks

1425

1426 **Declaration of interests**

1427

1428 ☒ The authors declare that they have no known competing financial interests or personal

1429 relationships that could have appeared to influence the work reported in this paper.

1430

1431 ☐ The authors declare the following financial interests/personal relationships which may be
1432 considered as potential competing interests:
1433

1434
1435

1436

LOCALITY	WELL		DEPTH (m)	LON GITUDE		LAT ITUDE	EINS	M ASS. MIN.
Taghouni	-		-80/-120	1'35"N	30°3	5'48"W	6°5	
Bou Azzer Centre	P 3		-420	1'13"N	30°3	4'48"W	6°5	✓
Bou Azzer East	P 3	302	-320/-	0'59"N	30°3	3'44"W	6°5	✓
Bou Azzer East	P 6		-510		30°3		6°5	✓

1437
1438

			0'57"N	3'35"W	
Aghbar	P 100	-325/-365/-405	30°3 1'35"N	6°4 9'06"W	✓
Oumlil	-	-77	30°3 1'22,55"N	6°4 7'6,89"W	
Bouismass	P 2	-390	30°3 0'55"N	6°4 7'18"W	✓
Bouismass	P 1	-80	30°3 0'59"N	6°4 5'15"W	✓
Tamdrost	-	-20	30°3 1'23.9"N	6°4 7'06.8"W	
Aït Ahmane					
Filon 53	-	-115/-200/-240	30°2 8'01"N	6°3 5'16"W	✓
Zone D	-	-200	30°2 9'50"N	6°3 7'21"W	
Quarries					
Bou Azzer Est	-	surface	30°3 1'01.8"N	6°5 3'41.2"W	
Filon 52	-	surface	30°2 8'15"N	6°3 5'41"W	✓
Filon 55	-	surface	30°3 1'22"N	6°4 7'13"W	✓
Surface					
Filon 2	-	surface	30°3 1'24.4"N	6°5 4'32.5"W	✓
Filon7 and *Filon 5* (*Bou Azzer Centre*)	-	surface	30°3 1'13"N	6°5 4'48"W	
Ambed	-	surface			
Trench					
Bou Azzer Est trench	-	surface	30°3 1'15.7"N	6°5 3'46.8"W	

1439

1440

1441

1442   Appendix

1443

1444   Appendix 1.1: Structural data on the direction to the north, the dip angle and the dip angle

1445   orientation of the massive mineralisation

Massive mineralisation	**Direction**	**Dip angle**	**Dip angle orientation**
BAE P6 (-510m)	N60	60	SE
BAE P6 (-510m)	N100	70	SE
Filon 53 (-145m)	N90	60	N
Aghbar (-365m)	N10	60	W

Bouismass (-390m)	N1 00	30	S
Aghbar (-325m)	N4 0	60	NW
Filon 53 (-240m)	N7 0	75	SE
BAE P3 (-320m)	N1 05	50	SSW

1446

1447   Appendix 1.2: Structural data on the direction to the north, the dip angle and the dip angle

1448   orientation of the veins system

Vein system	Direction	Dip angle	Dip angle orientation
BAC P3 (-420m)	N0 0	40	W
BAC P3 (-420m)	N1 0	60	W
BAE P6 (-510m)	N1 0	70	E
BAE P6 (-510m)	N1 0	70	W
BAE P6 (-510m)	N1 0	70	W
BAE P6 (-510m)	N1 0	85	E
BAE P6 (-510m)	N1 0	85	E
BAE P6 (-510m)	N1 00	30	S
BAE P6 (-510m)	N1 05	50	SSW
Taghouni (-80m)	N1 20	60	NE
Taghouni (-80m)	N1 20	75	NE
Taghouni (-80m)	N1 30	70	SW
Taghouni (-80m)	N1 35	40	SW
Taghouni (-80m)	N1 60	34	WSW
Aghbar (-365m)	N1 60	60	W
Bouismass (-390m)	N1 60	60	WSW
Bouismass (-390m)	N1 60	80	WSW
Bouismass (-80m)	N1 70	80	W
Bouismass (-80m)	N1 70	90	
Bouismass (-	N1	90	W

80m)	70		
Bouismass (-80m)	N1 74	70	ENE
Bouismass (-80m)	N1 75	85	E
Taghouni (-80m)	N2 0	60	W
Filon 7 - surface	N2 0	80	W
BAE P3 (-302m)	N2 2	88	W
BAE P3 (-302m)	N3 0	60	NW
BAE P3 (-302m)	N3 0	60	SE
BAE P3 (-302m)	N3 5	80	NW
Oumlil (-77m)	N4 0	50	NW
Tamdrost (-20m)	N4 0	60	NW
Zone D (-200m)	N4 0	60	NW
Zone D (-200m)	N4 0	60	NW
BA centre P3	N4 0	60	NW
BA centre P3	N4 0	65	SE
Filon 53 (-200m)	N4 0	70	SE
Filon 53 (-115m)	N4 0	80	NW
Filon 55 - surface	N4 0	80	NW
Filon 52 - surface	N4 5	85	NW
BAE P3 (-302m)	N5 0	80	NW

1449

1450

1451   Appendix 2: signal in Raman spectrometry and associated peaks of lizardite/chrysotile

1452   serpentinite
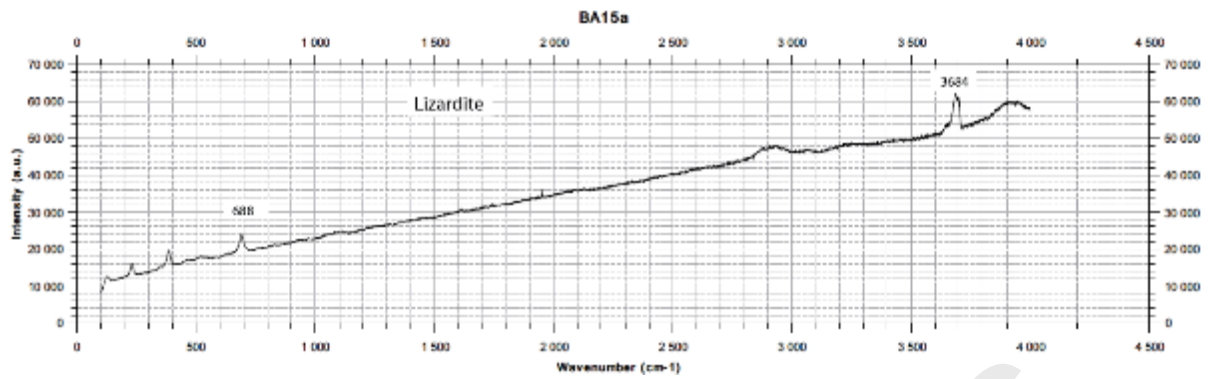
1453

1454   Appendix 3: As concentration of common rocks and minerals and from Bou Azzer

Rocks and minerals	As concentration (ppm)	Source
Oxide minerals		
Fe oxide (undifferentiated)	up to 2000	Boyle and Jonasson (1973)
Magnetite	2.7 - 41	Baur and Onishi (1969)
fibrous magnetite	400	Leblanc (1975)
magneite veins	20	Gahlan et al. (2006)
Silicate minerals		
Quartz	0.4-1.3	Baur and Onishi (1969)
Feldspar	<0.1-2.1	Baur and Onishi (1969)
Biotite	1.4	Baur and Onishi (1969)
Amphibole	1.1-2.3	Baur and Onishi (1969)
Olivine	0.08-0.17	Baur and Onishi (1969)
Pyroxène	0.05-0.8	Baur and Onishi (1969)
sulphide in serpentinite	50 and 1000	Leblanc &Fischer (1990)
Carbonate minerals		
Calcite	1 to 8	Boyle and Jonasson (1973)
Dolomite	<3	Boyle and Jonasson (1973)
Igneous rocks		
Apatite	<1 - 1000	Baur and Onishi (1969)
ultrabasic (peridotite, dunite, kimberlite, etc…)	0.03-15.8	smedley et al. (2002)
Serpentinized ultramafic rocks	10 - 450	Hattori et al. (2005); Sullivan (2007)
basalt	0.18-113	smedley et al. (2002)
gabbros	0.06-28	Onishi and Sandell (1955)
diorite, granodiorite	0.09-13.4	Boyle and Jonasson (1973)
rhyolite	3.2-5.4	Ure and Berrow (1982)
Neoproterozoic granitoid intrusions	<10 to ~25	Beraaouz et al. (2004)
Sedimentary rocks		
sandstone	0.6-120	Onishi and Sandell (1955)
Volcanic rocks		
ouarzazate group	100 - 300	Leblanc & Billaud (1982)

1455

1456

1457